Markov State Models and Perturbation-Based Approaches Reveal Distinct Dynamic Signatures and Hidden Allosteric Pockets in the Emerging SARS-Cov-2 Spike Omicron Variant Complexes with the Host Receptor: The Interplay of Dynamics and Convergent Evolution Modulates Allostery and Functional Mechanisms

Sian Xiao,

Department of Chemistry, Center for Research Computing Center for Drug Discovery, Design, and Delivery (CD4), Southern Methodist University, Dallas, Texas 75275, United States

Mohammed Alshahrani,

Keck Center for Science and Engineering, Schmid College of Science and Technology, Chapman University, Orange, California 92866, United States

Grace Gupta,

Keck Center for Science and Engineering Schmid College of Science and Technology, Chapman University, Orange, California 92866, United States

Peng Tao,

Department of Chemistry, Center for Research Computing, Center for Drug Discovery, Design, and Delivery (CD4), Southern Methodist University, Dallas, Texas 75275, United States

Gennady Verkhivker

Keck Center for Science and Engineering Schmid College of Science and Technology, Chapman University, Orange, California 92866, United States; Department of Biomedical and

Corresponding Authors: **Peng Tao** – *Department of Chemistry, Center for Research Computing, Center for Drug Discovery, Design, and Delivery (CD4), Southern Methodist University, Dallas, Texas 75275, United States;* ptao@smu.edu; **Gennady Verkhivker** – *Keck Center for Science and Engineering Schmid College of Science and Technology, Chapman University, Orange, California 92866, United States; Department of Biomedical and Pharmaceutical Sciences, Chapman University School of Pharmacy, Irvine, California 92618, United States.*

Pharmaceutical Sciences, Chapman University School of Pharmacy, Irvine, California 92618, United States

Abstract

The new generation of SARS-CoV-2 Omicron variants displayed a significant growth advantage and increased viral fitness by acquiring convergent mutations, suggesting that the immune pressure can promote convergent evolution leading to the sudden acceleration of SARS-CoV-2 evolution. In the current study, we combined structuralmodeling, microsecond molecular dynamics simulations, and Markov state models to characterize conformational landscapes and identify specific dynamic signatures of the SARS-CoV-2 spike complexes with the host receptor ACE2 for the recently emerged highly transmissible XBB.1, XBB.1.5, BQ.1, and BQ.1.1 Omicron variants. Microsecond simulations and Markovian modeling provided a detailed characterization of the functional conformational states and revealed the increased thermodynamic stabilization of the XBB.1.5 subvariant, which can be contrasted to more dynamic BQ.1 and BQ.1.1 subvariants. Despite considerable structural similarities, Omicron mutations can induce unique dynamic signatures and specific distributions of the conformational states. The results suggested that variant-specific changes of the conformational mobility in the functional interfacial loops of the receptor-binding domain in the SARS-CoV-2 spike protein can be fine-tuned through crosstalk between convergent mutations which could provide an evolutionary path for modulation of immune escape. By combining atomistic simulations and Markovian modeling analysis with perturbation-based approaches, we determined important complementary roles of convergent mutation sites as effectors and receivers of allosteric signaling involved in modulation of conformational plasticity and regulation of allosteric communications. This study also revealed hidden allosteric pockets and suggested that convergent mutation sites could control evolution and distribution of allosteric pockets through modulation of conformational plasticity in the flexible adaptable regions.

Graphical Abstract
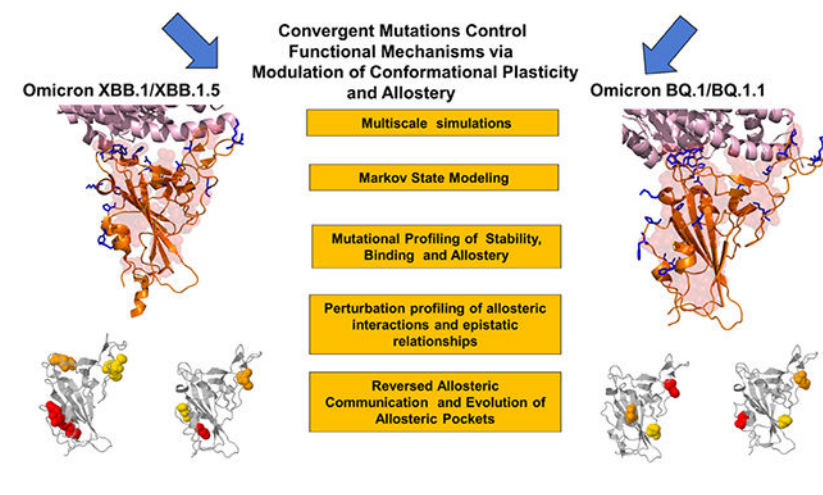
INTRODUCTION

A vast number of structural and biochemical studies have extensively explored the mechanisms underlying SARS-CoV-2 infection.[1–9] These investigations have unequivocally demonstrated the critical significance of the viral spike (S) glycoprotein in various aspects of the virus's life cycle, including virus transmission and immune evasion. The S glycoprotein has been identified as a key player in facilitating virus entry into host cells, allowing for viral replication and dissemination. Additionally, it plays a crucial role in evading the host immune response by employing various strategies, such as shielding important epitopes and modulating immune recognition.[1–9] The architecture of the S protein of SARS-CoV-2 is intricate, comprising an N-terminal S1 subunit and a C-terminal S2 subunit that is structurally rigid. The S1 subunit undergoes functional movements that involve conformational changes between the closed and open S states. These transitions are facilitated by coordinated global movements of the S1 subunit, which includes the N-terminal domain (NTD), receptor-binding domain (RBD), and two structurally conserved subdomains, SD1 and SD2. Together, these components dictate the S protein's structuraland dynamic response to binding partners and the ACE2 host receptor.[10–15]

Structural and biophysical studies have provided extensive characterization of the thermodynamic and kinetic properties of the functional SARS-CoV-2 S trimer.[16–18] These studies have focused on exploring the complex interplay between subdomain movements and long-range interactions that link the S1 and S2 subunits to regulate the equilibrium and population shifts of the RBD between the open (up) and closed (down) conformations. The RBD serves as the primary site of interaction between the S protein and the ACE2 receptor on host cells and the population shifts of the RBD between open and closed conformations directly impact the accessibility of the ACE2 binding site. The exposure of the RBD in the open conformation can enhance the interaction between the S protein and ACE2, resulting in a higher binding affinity, while when the RBD is in the closed conformation, the binding affinity may be weakened or inhibited. This regulatory mechanism allows the S protein to finely modulate its interaction with ACE2 and determine the efficiency of viral entry into host cells.[16–18] The receptor-binding motif (RBM) is the main functional motif in RBD[16–18] and is composed of the RBD residues 437–508 that form the binding interface between the RBD and ACE2 (Supporting Materials, Figure S1). The recognition loop residues (residues 470–491) of the RBM form a dense interaction network with the ACE2 receptor that determines the RBD-ACE2 binding affinity providing a molecular link with virus infectivity.

Cryo-electron microscopy (cryo-EM) and X-ray structural studies have been instrumental in elucidating structural characteristics of the SARS-CoV-2 S protein variants of concern (VOCs) in different functional states, as well as their complexes with antibodies.[19–28] These investigations have unveiled a remarkable diversity of binding epitopes and highlighted the versatility of the S protein's binding mechanisms when interacting with various classes of antibodies. Biophysical studies using the differential scanning fluorimetry (DSF) assay have investigated the protein stability of SARS-CoV-2 Wu-Hu-1, Delta, and Omicron variants, showing that the S Omicron BA.1 variant exhibits the lower inflection temperature and a reduced protein stability for the S Omicron BA.1 variant compared to the S Wu-Hu-1 and S Delta variants, while the BA.2 RBD was found to be more stable than the BA.1

variant.[29–32] In contrast to the conformational changes observed in the original Wu-Hu-1 strain and other VOCs upon ACE2 binding, the Omicron S protein exhibits a distinct behavior showing a preference for the "one-RBD-up" conformation both before and after ACE2 binding.[33–35] The Omicron BA.2 subvariants of SARS-CoV-2 have been linked to the increased transmissibility and especially significant antibody and vaccine evasion capabilities.[36–40] Studies examining the binding affinities of Omicron BA.1.1 and BA.2 with the ACE2 receptor revealed that these variants exhibit stronger binding affinity compared to the BA.3 and BA.1 variants, suggesting that these variants may have a higher potential for viral entry into host cells.[41–43] At the same time, surface plasmon resonance (SPR) studies showed that the Omicron BA.4/5 RBD has only marginally greater binding affinity for ACE2 compared to the ancestral Wu-Hu-1 strain and the BA.1 variants.[44] The cryo-EM structures and biochemical analysis of the S trimers for BA.1, BA.2, BA.3, and BA.4/BA.5 subvariants confirmed that the increased transmissibility of the BA.2 variant can be driven by a combination of the enhanced ACE2 binding affinity and stronger antibody evasion compared to the other Omicron sublineages.[45,46] The cryo-EM conformations of the BA.2.75 S trimer in the open and closed forms, as well as the structures of the open BA.2.75 complexes with ACE2, have shown that the BA.2.75 is the most stable among the Omicron variants, exhibiting ~4–6-fold increased binding affinity compared to other Omicron variants.[47,48]

The BA.2 variant generated a new wave that led to a second generation of newly emerging Omicron variants that display a significant growth advantage and include BA.2.3.20, BA.2.75, BQ.1, BQ.1.1 XBB.1, XBB.1.5, and XBB.1.6 subvariants.[49,50] They demonstrated the increased transmissibility and the ability to outcompete other strains in the rate of infectivity and spread.[50] The XBB.1 subvariant is derived from the BA.2 lineage and emerged by recombination of two cocirculating BA.2 lineages (BJ.1 and BM.1.1.1). The XBB.1.5 subvariant harbors F486P modification involving a two nucleotide substitution, and while it is equally immune-evasive to closely related XBB.1 with F486S mutation, XBB.1.5 exhibits growth advantage due to the higher ACE2 binding affinity from a single S486P mutation that can restore most of the favorable hydrophobic contacts.[51–53] These studies suggested that R346T and L368I substitutions may enhance binding affinity, while F486S in XBB.1 leads to the decreased ACE2 binding affinity. BQ.1 is a direct descendant of BA.5, with additional spike mutations in some key antigenic sites (K444T and N460K). Its first descendant, BQ.1.1 carries a further additional mutation R346T. Biochemical investigations demonstrated that the binding affinity of the XBB RBD can be enhanced compared to that of the BA.2 variant but is weaker than for the BA.2.75 variant.[53,54] At the same time, the binding affinities for BQ.1 and BQ.1.1 were comparable to the binding exhibited by the BA.4/5 variants.[53,54] The binding affinity of the XBB.1.5 RBD-ACE2 was only slightly weaker than the one observed for BA.2.75 but significantly stronger than that of the XBB.1 and BQ.1.1 variants.[55] The neutralizing activity against XBB.1.5 was markedly lower than immune evasion of the ancestral strain and BA.2, while similar immune escape potential was observed for the XBB.1 and XBB.1.5 variants.[56,57] These studies concluded that a high transmissibility and rapid surge of the newly emerged variants may result from the considerably enhanced immune evasion potential and the preserved favorable ACE2 binding, leading to the improved fitness which is comparable only to the BA.2.75 variant.

Since March 2023, sublineages of the XBB variant harboring the F486P substitution (XBB.1.5 and XBB.1.9) dominated worldwide (https://nextstrain.org/ncov/gisaid/global/6m). Very recently, an XBB sublineage XBB.1.16 RBD emerged in various countries including the US. Compared to XBB.1.5, XBB.1.16 has E180V and T478R mutations showing a greater growth advantage in the human population compared to XBB.1 and XBB.1.5 variants, while exhibiting similar immune evasion potential.[58] The emerging variants display the increased infectivity and transmissibility over previous Omicron variants, and some RBD residues (R346, K356, K444, V445, G446, N450, L452, N460, F486, F490, R493, and S494) are mutated in at least five new independent Omicron sublineages.[59] BQ.1.1 subvariant bears all five recent convergent mutations (R346T, K444T, L452R, N460K, and F486V). Evolutionary studies suggested that sublineages descending from BA.5, including BQ.1 and BQ.1.1 convergently increased viral fitness by consecutively acquiring substitutions at the R346, N460, and K444 residues, and it was proposed that BQ.1.1 increased the binding affinity to human ACE2 during evolution from the BA.5 variant.[60] Consistent with previous studies from the same group[51,52] L452R and N460K substitution can increase the ACE2 binding affinity, while K444T substitution significantly decreased ACE2 binding affinity.[60] It was suggested that acquiring L452R and N460K substitutions that potentially increase ACE2 binding ability can allow for the increased substitution frequency at the convergent sites to modulate immune escape capacity. Indeed, the latest studies showed that several convergent mutations present in the BA.2 or BA.5 subvariants including R346T mutation that was found in BA.2.75.2, as well as K444T and N460K substitutions can be associated with the robust escape from monoclonal antibodies and from vaccine-induced antibodies.[61,62] The patterns of convergent evolution in the Omicron variants was reviewed recently using analysis of the mutations which emerged at least three times independently in different linages.[63] The convergently evolved mutations tend to cluster in specific locations of the NTD and RBD, and spatial clustering under convergent evolution is believed to create potential synergic binding effects between the RBD mutations.[64,65] Additionally, convergent mutations N439K, N440K, L452R, T478R/K, and E484K may have evolved to carry positive charges, thus enhancing the electrostatic complementarity with the ACE2. Importantly, balancing the ACE2 binding and immune escape fitness tradeoffs can shape up the RBD evolution and patterns of convergent mutations. By examining mechanisms driving the emergence of convergent RBD mutations, it was suggested that the immune pressure on the RBD becomes increasingly focused and promotes convergent evolution, explaining the observed sudden acceleration of SARS-CoV-2 RBD evolution and the convergence pattern.[66]

Computer simulations of the SARS-CoV-2 S proteins have allowed for a better understanding of the molecular mechanisms of SARS-CoV-2 S protein and receptor binding. Molecular dynamics (MD) simulations of the full-length SARS-CoV-2 S glycoprotein embedded in the viral membrane with a complete glycosylation profile provided detailed characterization of the conformational landscapes of the S proteins in the physiological environment.[67–70] Using distributed cloud-based computing, large-scale MD simulations of the viral proteome observed dramatic opening of the S protein complex, predicting the existence of several cryptic epitopes in the S protein.[71] MD simulations of the S protein in solution and targeted simulations of conformational changes between the open

and closed S forms revealed the key electrostatic interdomain interactions mediating the protein stability and kinetics of the functional spike states.[72] Using the replica-exchange MD simulations, conformational landscapes of the full-length S protein trimers were investigated, unveiling hidden functional intermediates along with open-closed transition pathways and previously unknown cryptic pockets.[73] Using MD simulations with a full representation of glycan moieties, conformational changes in a complete membrane-embedded SARS-CoV-2 spike glycoprotein were probed to accurately describe pocket dynamics leading to discovery of cryptic pockets.[74] The linkage between conformational dynamics and allosteric modulation of SARS-CoV-2 S in the absence or presence of ligands was established in an smFRET imaging assay, showing the presence of long-range allosteric control of the RBD equilibrium, which in turn regulates the exposure of the binding site and antibody binding.[18] Our studies used integrative computational modeling approaches to reveal that the S protein could function as an allosteric regulatory machinery controlled by stable allosteric hotspots acting as drivers and regulators of spike activity.[75–81] A comparative analysis of the conformational dynamics, electrostatics, protein stability, and allostery in the different functional states of S trimers for BA.1, BA.2, and BA.2.75 variants showed that Omicron mutations may evolve by targeting vulnerable sites of conformational adaptability to elicit immune escape while maintaining their control on balancing protein stability and functional fitness through robust allosteric communications with the stability hotspots.[82] By combining atomistic simulations and a community-based network model of epistatic couplings, we found that convergent Omicron mutations such as G446S (BA.2.75, BA.2.75.2, XBB), F486V (BA.4, BA.5, BQ.1, BQ.1.1), F486S, F490S (XBB.1), F486P (XBB.1.5) can display epistatic relationships with the major stability and binding affinity hotspots which may allow for the observed broad antibody resistance.[83]

In the current study, we perform multiple microsecond MD simulations and Markov state model (MSM) analysis to characterize conformational landscapes and identify specific dynamic signatures of the SARS-CoV-2 S RBD-ACE2 complexes for the recently emerged XBB.1, XBB.1.5, BQ.1, and BQ.1.1 Omicron variants. The results of simulations and MSM analysis provide a detailed characterization of the conformational states in the Omicron complexes, showing the increased thermodynamic stabilization of the XBB.1.5 complex, which is contrasted to more dynamic BQ.1 and BQ.1.1 variants. Using a comparative MSM analysis, we discover variant-specific changes of conformational mobility in the flexible RBD loops 470–491 and 440–452 containing convergent mutation sites that allow for modulation of conformational plasticity and immune escape.

By combining MSM analysis with perturbation-based response approaches, we also examine mechanisms of long-range dynamic couplings and allosteric communications in the Omicron RBD-ACE2 complexes. Based on the premise that allostery is linked with the evolvability of proteins, we explore the relationship between allosteric interactions and patterns of convergent Omicron mutations, showing how convergent mutations can potentiate conformational plasticity and modulate allosteric responses in the RBD to binding and immune escape. Using perturbation response scanning analysis, our study reveals important complementary roles of convergent Omicron mutations as regulators and transmitters of allosteric signaling in the RBD-ACE2 complexes. By integrating the results of atomistic MD simulations and MSM analysis with perturbation-based profiling of

allosteric residue potentials, we characterize the conformational landscape of the Omicron RBD-ACE2 complexes and examine the effect of Omicron mutations on the thermodynamic stability and kinetic transitions between different conformational states. Our findings suggest a mechanism in which convergent Omicron mutations can promote high transmissibility and antigenicity of the virus by controlling the interplay between the RBD stability and conformational adaptability, allowing for optimal fitness tradeoffs between binding to the host receptor and robust immune evasion profile. We also explore our method for fast and accurate allosteric site prediction PASSer (Protein Allosteric Sites Server) (https://passer.smu.edu)[84–87] to characterize the distribution allosteric sites in the Omicron complexes and detect previously unknown hidden allosteric pockets present in the stable RBD conformations. Through integrative computational approaches, this study provides a systematic analysis and comparison of the effects of Omicron subvariants on conformational dynamics and allosteric signaling in the complexes with the ACE2 receptor.

MATERIALS AND METHODS

Structural Modeling and Refinement.

The crystal structures of the BA.2 RBD-ACE2 (pdb id 7XB0) and BA.5 RBD-ACE2 complexes (pdb id 7XWA) were obtained from the Protein Data Bank.[88] During structure preparation stage, protein residues in the crystal structures were inspected for missing residues and protons. Hydrogen atoms and missing residues were initially added and assigned according to the WHATIF program web interface.[89] The missing loops in the studied cryo-EM structures of the SARS-CoV-2 S protein were reconstructed and optimized using the template-based loop prediction approach ArchPRED.[90] The side-chain rotamers were refined and optimized by the SCWRL4 tool.[91] The protein structures were then optimized using atomic-level energy minimization with composite physics and knowledge-based force fields implemented in the 3Drefine method.[92] The protonation states of the titratable residues of the ACE2 and RBD proteins were predicted at pH 7.0 using Propka 3.1 software using the PROPKA software and web server,[93] and the titratable residues were assigned the dominant protonation state at pH 7.0.

The refined structural models of the XBB.1 RBD-ACE2 and XBB.1.5 RBD-ACE2 complexes were obtained based on its paternal BA.2 RBD-ACE2 complex, and the models for BQ.1 and BQ.1.1 complexes were constructed based on the paternal BA.5 RBD-ACE2 complex. The MutaBind2 approach was employed to introduce mutations and optimize structural models for XBB.1, XBB.1.5, BQ.1, and BQ.1.1 RBD-ACE2 complexes.[94,95] This approach utilizes the FoldX energy model[96,97] to introduce single or multiple point mutations on the crystal structure, followed by robust side-chain optimization and multiple rounds of energy minimization using the NAMD 2.9 program[98] with the CHARMM36m force field.[99]

All-Atom Molecular Dynamics Simulations.

The CHARMM36M force field[99] with the TIP3P water model[100] was employed to perform all-atom MD simulations for each of the Omicron RBD-ACE2 complexes. The structures of the SARS-CoV-2 S-RBD complexes were prepared in Visual Molecular Dynamics (VMD

1.9.3).[101] The protonation states of titratable residues were determined under neutral pH. The protein systems were solvated in 130 Å × 85 Å × 75 Å water boxes. In each system, sodium and chloride ions were added to maintain an ionic strength of 0.1 M. After energy minimization, the systems were first heated up from 100 to 300 K with a temperature increment of 20 K per 50 picoseconds (ps). Consequently, the systems were subjected to 1.5 nanoseconds (ns) isothermal–isobaric (NPT) equilibrations at 300 K (equilibrium run), followed by 1 microsecond (μs) canonical (NVT) simulations (production run) at 300 K. Snapshots of the production run were saved every 100 ps. In all simulations, the SHAKE constraint was used to constrain bonds associated with hydrogen atoms in the solvent molecules and the proteins.[102] The nonbonding interactions within 10 Å were calculated explicitly. The Lennard-Jones interactions were smoothed out to zero at 12 Å. The long-range electrostatic interactions were calculated using the particle mesh Ewald method[103] using a fourth order (cubic) interpolation and a cutoff of 10.0 Å. The simulations were conducted using OpenMM (version 7.6.0).[104] For each system, MD simulations were conducted three times in parallel to obtain comprehensive sampling. Each individual simulation has 10,000 frames.

For each system, MD simulations were conducted three times in parallel to obtain comprehensive sampling. Each individual simulation of the studied BA.2, BA.4/BA.5, XBB.1, XBB.1.5, BQ.1, and BQ.1.1 RBD-ACE2 complexes stored 10,000 frames; thus, we collected 30,000 frames for each of the complexes.

Time-Structure-Based Independent Component Analysis.

The time-structure independent components analysis (tICA) method identifies the slowest degrees of freedom and can preserve the kinetic information present in the MD trajectories by maximizing the autocorrelation function.[105–108] In contrast to principal component analysis (PCA), which finds coordinates of maximal variance, tICA finds coordinates of maximal autocorrelation at the given lag time. Therefore, the tICA approach is useful to find the slow components in a data set and a robust method to transform MD simulation information before clustering data for the construction of a Markov model. Using a time series of molecular coordinates provided by an n-dimensional MD trajectory $x(t) = (x_1(t), \cdots, x_n(t))^T \in \mathbb{R}^n$ with Cartesian coordinates $(x_1, \cdots, x_n)$, tICA can reduce the dimensionality of the trajectories and determine the slowest independent collective degrees of freedom onto which the projections of the initial data set have the largest time autocorrelation.

The tICA approach identifies the slowest degrees of freedom by solving the generalized eigenvalue problem:

$$\bar{C}F = CFK$$

(1)

where $K = \operatorname{diag}(k_1, \cdots, k_n)$ and $F = (f_1, \cdots, f_n)$ are the eigenvalue and eigenvector matrices, respectively, and C and $\bar{C}$ are the covariance matrix and the time-lagged covariance matrix of the coordinate vector defined as follows, respectively,

$$C = \left\langle (x((t) - \langle x(t) \rangle)^T (x(t) - \langle x(t) \rangle) \right\rangle$$

(2)

$$\bar{C} = \left\langle (x(t) - \langle x(t) \rangle)^T (x(t + t_0) - \langle x(t) \rangle) \right\rangle$$

(3)

where $\langle \cdots \rangle$ denotes the average. In order to obtain a symmetric time-lagged covariance matrix, $\frac{1}{2}(\bar{C} + \bar{C}^T)$ is calculated. The latter step assumes the time reversibility of the process, which is satisfied in MD simulations. The featurization and dimensionality reduction were performed using the PyEMMA package.[109]

Markov State Model.

Stochastic Markov state models (MSMs)[110–112] have become increasingly useful states-and-rates models with the mature and robust software infrastructure[113,114] for describing the transitions between functional protein states and modeling of allosteric events. In MSM, protein dynamics is modeled as a kinetic process consisting of a series of Markovian transitions between different conformational states at discrete time intervals. A specific time interval, referred to as the lag time, needs to be determined to construct a transition matrix. First, k-means clustering method is conducted on projected low-dimensional space and each simulation frame is assigned to a microstate. The transition counting is constructed based on a specific time interval lag time τ. Macrostates are kinetically clustered based on the Perron-Cluster Cluster Analysis (PCCA++)[115] and considered to be kinetically separate equilibrium states. The transition matrix and transition probability were calculated to quantify the transition dynamics among macrostates. The corresponding transition probability from state i to state j is calculated as

$$P_{ij}(\tau) = \text{Prob}(X_t + \tau \in S_j \mid X_t \in S_i)$$

(4)

A proper lag time is required for MSM to be Markovian. The value of the lag time and the number of macrostates are selected based on the result of estimated relaxation timescale.[116] The implied timescales can be calculated using the eigenvalues (λ_i) in the transition matrix as

$$t_i = -\frac{\tau}{\ln|\lambda_i(\tau)|}$$

(5)

The number of protein metastable states associated with these slow relaxation timescales can be inferred based on the convergence of the implied relaxation timescale. These metastable states effectively discretize the conformational landscape. The Markov state model building was conducted using the PyEMMA package (v2.5.12).[109] Based on the transition matrix, we

obtain implied timescales for transitioning between various regions of phase space and use this information to determine the number of metastable states. The number of metastable states also defines the resolution of the model by determining how large a barrier must be in order to divide phase space into multiple states.

Perturbation Response Scanning.

The perturbation response scanning (PRS) approach[117–120] performed in the current study implemented the protocol originally proposed by Bahar and colleagues[121,122] and was described in detail in our previous studies.[123,124] In this approach, it is the 3N × 3N Hessian matrix H (N is the number of nodes/residues in the protein) whose elements represent second derivatives of the potential with respect the coordinates of each protein node, thus connecting the perturbation forces to the residue displacements. The 3N-dimensional vector ΔR of the node displacements in response to 3N-dimensional perturbation force follows Hooke's law $F = H * \Delta R$.

In the PRS approach, a perturbation force of a given magnitude is applied to one residue at a time, and the response of the protein system is measured. The force exerted on residue i is expressed as

$$F^{(i)} = (0\ 0\ 0 \cdots F_x^{(i)}\ F_x^{(i)}\ F_x^{(i)} \cdots 0\ 0\ 0)^T$$

(6)

The resulting response is measured by the displacement vector:

$$\Delta R(i) = H^{-1} F^{(i)}$$

(7)

The second derivatives matrix H is obtained from simulation trajectories for each protein structure, with residues represented by C_a atoms. The deviation of each residue from an average structure is calculated by $\Delta R_j(t) = R_j(t) - \langle R_j(t) \rangle$ and the corresponding covariance matrix C is then calculated by $\Delta R \Delta R^T$. We sequentially perturbed each residue in the SARS-CoV-2 spike structures by applying a total of 250 random forces to each residue to mimic a sphere of randomly selected directions. The displacement changes, ΔR^i is a 3N-dimensional vector describing the linear response of the protein and deformation of all of the residues. Using the residue displacements upon multiple external force perturbations, we compute the magnitude of the response of residue k as $\langle || \Delta R_k^{(i)} ||^2 \rangle$ averaged over multiple perturbation forces $\mathbf{F}^{(i)}$, yielding the ikth element of the N × N PRS matrix. The average effect of the perturbed effector site i on all other residues is computed by averaging over all sensor (receiver) residues j and can be expressed as $\langle (\Delta R^i)^2 \rangle_{effector}$. The effector profile determines the global influence of a given residue node on the perturbations in other protein residues and can be used as proxy for detecting allosteric regulatory hotspots in the interaction networks. In turn, the jth column of the PRS matrix describes the sensitivity

profile of sensor residue j in response to perturbations of all residues, and its average is denoted as $\left\langle (\Delta R^i)^2 \right\rangle_{sensor}$. The sensor profile measures the ability of residue j to serve as a receiver of dynamic changes in the system.

Machine Learning-Based Prediction of Allosteric Pockets.

Machine learning can help detect and predict allosteric sites in proteins since it can deal with numerous input features, including local or static features of pockets and delocalized or dynamic features of proteins.[125] In the current study, we employed the recently developed PASSer approach that provides fast and accurate predictions of allosteric sites in proteins.[84–87] PASSer offers three pretrained machine learning-based models: (a) an ensemble learning model consisting of extreme gradient boosting (XGBoost) and a graph convolutional neural network (GCNN),[84] (b) an automated machine learning model powered by AutoGluon from Amazon Web Services (AWS),[85] and (c) a learning-to-rank (LTR) model.[86] The PASSer web server has been widely used for the validation of known functional pockets and the discovery of new allosteric sites.[87]

Here, we used the LTR model capable of ranking binding pockets and identifying the most probable allosteric binding sites.[86] The LTR model in PASSer was trained and validated on two widely used data sets, the Allosteric Database (ASD)[126,127] which is a comprehensive database of allosteric proteins and modulators and CASBench which is a benchmarking set that includes annotated catalytic and allosteric sites.[128] FPocket is used in this approach to detect protein binding pockets and calculate physical and chemical features.[129] All pockets in the protein were ranked according to their likelihood to be allosteric protein sites using the pretrained LTR algorithm with LightGBM, which is a highly efficient gradient boosting decision tree approach[130] and the LambdaMART method. LambdaMART combines gradient boosting decision tree (GBDT) with the loss function derived from LambdaRank, an LTR algorithm.[86]

RESULTS AND DISCUSSION

Microsecond MD Simulations of the Omicron RBD-ACE2 Complexes Reveal Distinct Dynamic Signatures of RBD Proteins.

We first performed a comparative structural analysis of the Omicron RBD-ACE2 complexes for XBB.1 and XBB.1.5 complexes with the ACE2 receptor (Figure 1). Mutations G339D, S373P, S375F, K417N, N440K, S477N, T478K, E484A, Q493R, Q498R, N501Y, and Y505H in BA.2 are shared with the BA.1 variant, but BA.2 additionally carries S371F, T376A, D405N, and R408S mutations (Table 1). The BA.2.75 subvariant has nine additional mutations compared to BA.2 in the NTD (K147E, W152R, F157L, I210V, and G257S) and RBD (D339H, G446S, N460K, and R493Q) (Table 1). G446S mutation is shared with Omicron BA.1, and R493Q reversed mutation is present in BA.4/BA.5 as well as in XBB.1 and XBB.1.5 subvariants. The XBB.1 subvariant is a descendant of BA.2 and recombinant of BA.2.10.1 and BA.2.75 sublineages, featuring NTD mutations V83A, H146Q, Q183E, V213E, and G252V and specific RBD mutations (G339H, R346T, L368I, V445P, G446S, N460K, F486S, F490S, and reversed R493Q) (Table 1). Many of these RBD mutations

are known for their immune evasion functions, including R346T, G446S, and F486S.[57] XBB.1.5 is remarkably similar to XBB.1 with a critical single RBD modification F486P mutation (Table 1). Among the most recent descendant lineages, the Omicron subvariant BQ.1 is a direct descendant of BA.5, with additional spike mutations in some key antigenic sites (K444T and N460K). Its first descendant, BQ.1.1 carries a further additional mutation (R346T).[131,132] BQ.1 has been detected in 65 countries, with an overall prevalence of 6%.

Despite considerable mutational differences between newly emerged Omicron variants, structural analysis of the RBD complexes with ACE2 for these variants revealed highly similar RBD conformations and the same binding mode of interactions, rendering overall very minor differences in the crystallographic conformations (Figure 1). We conjectured that the regulatory mechanisms of Omicron variants and functional differences in stability, binding, and immune escape can be examined through the lens of the conformational dynamics, reconstruction of the conformational landscape, and analysis of the distribution of multiple substates available to these systems. To characterize conformational landscapes and dynamic signatures of the Omicron variants, we conducted multiple independent microsecond MD simulations for each of the studied RBD-ACE2 complexes (Tables 1 and 2, Figure 2). MD simulations revealed important commonalities and striking differences in the intrinsic conformational dynamics of the RBDs among Omicron variants.

The conformational flexibility of the Omicron RBD was analyzed by calculating the root-mean-square deviations (RMSDs) (Supporting Materials, Figures S2,S3) and the root-mean-square fluctuation (RMSF) distribution for the RBD residues (Figure 2).

The RMSD profiles for the RBD residues showed a fast convergence of the MD trajectories, for the BA.2 and XBB.1.5 complexes where all three trajectories converged reaching a steady equilibrium state after about 350–400 ns (Supporting Materials, Figure S2). An appreciable divergence of the RMSD profiles was seen for the MD trajectories of the XBB.1 complex (Supporting Materials, Figure S2B,E) reflecting a more heterogeneous ensemble of the RBD conformations also pointing out to a greater flexibility of the ACE2.

The RMSD profiles for the Omicron BQ.1.1 RBD showed convergence of the three microsecond trajectories reaching the steady state after ~250–300 ns (Supporting Materials, Figure S3C). A more significant divergence among trajectories was detected for the parental BA.5 RBD (Supporting Materials, Figure S3A) and particularly BQ.1 RBD (Supporting Materials, Figure S3B). The RMSDs for the ACE2 displayed a certain degree of variability among trajectories for BA.5, BQ.1, and BQ.1.1 variants indicating the functionally significant plasticity of both binding partners in the RBD-ACE2 complexes. These preliminary findings also suggested that the RBD residues in the XBB.1 and BQ.1 variants may be more dynamic than in the very closely related XBB.1.5 and BQ.1.1 sublineages.

The RMSF profiles showed several local minima regions corresponding to the structured five-stranded antiparallel β-sheet core region (residues 350–360, 375–380, and 394–403). Common to the conformational mobility profiles that displayed a similar overall shape was the presence of two RMSF peaks corresponding to the flexible RBD regions (residues

360–373 and residues 380–396) (Figure 2). The RBD regions 440–456, 470–491, and 491–505 include a number of binding interface residues. In particular, residues 491–505 forming a dominant cluster of major interaction contacts with ACE2 consistently and displayed small fluctuations and featured considerable binding-induced stabilization in all complexes. Interestingly, the flexible RBD loops 440–452 and 470–491 containing many of the convergent mutation sites showed significant differences in their mobility across the Omicron variants (Figure 2).

The RMSF profiles revealed larger thermal fluctuations for the XBB.1 RBD (Figure 2A) compared to more stable XBB.1.5 RBD (Figure 2B). The increased rigidification of the XBB.1.5 RBD residue was manifested not only in the smaller deviations of the ACE2-interacting residues but also in only moderate displacements of the flexible RBD regions (residues 355–375 and 380–400) (Figure 2A,B). The stable RBD core regions (residues 390–420 and 430–450) exhibited even smaller fluctuations in the XBB.1.5 complex (Figure 2A,B), suggesting the increased RBD stability for these variants which may be a relevant contributing factor to the stronger ACE2 binding experimentally observed for the XBB.1.5 subvariant.[54,55] The RMSF profile for XBB.1.5 is characterized by several local minima corresponding to the rigid RBD core, the ACE2 interfacial sites (residues 485–505) (Figure 2B). Importantly, the thermal movements of the intrinsically more flexible RBM region were markedly suppressed in the XBB.1.5 variant (Figure 2B). The RBM tip in the XBB.1.5 RBD-ACE2 complex is maintained in a stable folded conformation that can be described as a hook-like folded motif that is similar to the crystallographic conformations. Interestingly, in the XBB.1 RBD, the RBM tip is more flexible and samples a more dynamic state that circulates between a variety of partly disordered RBM conformations (Figure 2A).

By constructing mutational models of BQ.1 and BQ.1.1 RBD-ACE2 complexes using the crystal structure of the BA.4/BA.5 complex and performing microsecond atomistic MD simulations, we observed several interesting patterns in the distributions. The RMSF profiles for the BQ.1 RBD residue showed markedly greater fluctuations (Figure 2C) compared to closely related BQ.1.1 RBD (Figure 2D). In particular, we noticed the reduced mobility in the RBM region and partly suppressed motions of intrinsically flexible RBM tip residues 475–486 in the BQ.1.1 (Figure 2D). Interestingly, convergent mutation sites R346T, K444T, and N460K belong to fairly exposed flexible regions, but these positions experienced only very moderate fluctuations in the BQ.1.1 RBD-ACE2 complex. One of the microsecond MD trajectories of the BQ.1.1 RBD-ACE2 complex showed some divergence in the RMSF values showing larger fluctuations of the convergent mutational positions K444, V445, and G446 (Figure 2D). The key Omicron mutational positions Q493R, Q498R, N501Y, and Y505H that participate in the critical ACE2 binding interface region are highly constrained by their strong interactions with the receptor and experience only very minor fluctuations across all of the studied variants. Overall, the major difference in the dynamic signatures between Omicron variants was a noticeable reduction in the mobility of the intrinsically flexible RBM loop for XBB.1.5 and BQ.1.1 subvariants, while this region is characterized by greater conformational variability and lack of the well-defined folded RBM tip in the XBB.1 and BQ.1 variants (Figure 2).

To provide a more detailed analysis of stable and flexible RBD regions, we used conformational ensembles and computed the fluctuations of the mean distance between each residue and all other protein residues. These variations can be converted into the distance fluctuation stability indexes to measure the energetics of the residue deformations.[133,134] The adaptation of this approach for the analysis of rigid and flexible residues in the SARS-CoV-2 S proteins was detailed in our previous studies.[83] In this approach, the high values of distance fluctuation stability indexes point to structurally rigid residues as they display small fluctuations in their distances to all other residues, while small values of this index would point to more flexible sites that display larger deviations of their inter-residue distances. A comparative analysis of the residue-based distance fluctuation profiles revealed several dominant and common peaks reflecting the similarity of the topological and dynamical features of the RBD-ACE2 complexes (Supporting Materials, Figure S4). The distributions showed that the local maxima for all RBD-ACE2 complexes are aligned with structurally stable and predominantly hydrophobic regions in the RBD core (residues 390–420 and 430–450). These peaks are particularly pronounced for the RBD residues in the XBB.1.5 RBD-ACE2 complex (Supporting Materials, Figure S4A). Somewhat smaller distance fluctuation stability indexes are featured for the RBD core residues in the more dynamic BQ.1 and BQ.1.1 complexes (Supporting Materials, Figure S4B). Notably, the ACE2 binding induced significant stabilization of the RBD residues 490–510 as evident from sharp peaks of the distribution for all complexes. This segment includes the RBM positions (residues 490–505) that are involved in direct interactions with ACE2 and determine the binding affinity of the RBD-ACE2 complexes. Notably, the RBD positions associated with the high distance fluctuation stability indexes are shared among all Omicron variant complexes, featuring conserved structural stability hotspots F400, I402, Y421, Y453, L455, F456, Y473, A475, and Y489 (Supporting Materials, Figure S4A). A similar shape of the stability index distributions for all Omicron variants suggested the conserved partition of stable and flexible RBD regions. Nonetheless, the larger peaks can be seen for the more stable XBB.1.5 complex (Supporting Materials, Figure S4A). This implies that the RBD core regions and ACE2 binding interface positions are considerably rigidified in the XBB.1.5 variant. Hence, our analysis further confirms the improved RBD stability of XBB.1.5 compared to the more dynamic BQ.1 and BQ.1.1 complexes. The structural rigidity and evolutionary conservation of Y449, Y473, L455, F456, and Y489 hotspots are critical for the stability and functionality of the RBD. By projecting sites of Omicron mutations on the stability index distributions (Supporting Materials, Figure S4), we found that these substitutions tend to target more dynamic and energetically tolerant sites, inducing moderate binding affinity changes while allowing for robust modulation and enhancement of immune escape potentials.

The RMSF analysis of the ACE2 residues showed similar profiles across all of the examined variants (Figure 3). The highly stable ACE2 residues corresponding to the rigid core and the binding interface positions are centered around K353 and H34 positions (Figure 3). The key ACE2 binding motifs correspond to an α-helix (residues 24–31) and a β-sheet (residues 350–356) that display moderate RMSF values in all complexes. The important polar charged residue interactions at the interface are formed with the ACE2 residues D30, K31, H34, and E35 that display small thermal fluctuations. Other ACE2 residues Q24, M82, Y83, D38, Y41, N330, and K353 that anchor distinct parts of the RBD-ACE2 binding interface

remained stable in all MD trajectories (Figure 3). Notably, the conformational dynamics profiles revealed signs of the increased ACE2 heterogeneity in the flexible loop (residues 340–350) which is located away from the binding interface, and this mobility increased in the XBB.1.5 and BQ.1.1 RBD-ACE2 complexes (Figure 3B,D).

Structural mapping of the conformational mobility profiles for the Omicron RBD-ACE2 complexes (Supporting Materials, Figure S5) underscored crucial differences in the rigidity and flexibility of the RBD residues, showing the enhanced stabilization of the RBD core in the XBB.1.5 variant (Supporting Materials, Figure S5B) compared to the less rigid XBB.1 complex (Supporting Materials, Figure S5A). The structural maps also demonstrated minor changes in the rigidity of the ACE2 regions, particularly for XBB.1.5 (Supporting Materials, Figure S5B) and BQ.1.1 variants (Supporting Materials, Figure S5D). For both complexes, the conformational dynamics profiles indicated further stabilization of the ACE2 regions that are distal from the RBD-ACE2 binding interface. At the same time, the RBD in the BQ.1.1 complex is more dynamic compared to the structurally rigid XBB.1.5 RBD. These observations may indicate that Omicron mutations in different variants could induce moderate and yet specific long-range response on both RBD-ACE2 binding interface contacts and also on long-range allosteric interactions.

To examine the character of dynamic couplings and quantify correlations between motions of the RBD regions, we performed the dynamic cross correlation (DCC) residue analysis and reported the DCC maps for the Omicron RBD-ACE2 complexes (Figure 4). The DCC maps demonstrated subtle differences in the dynamic couplings (Figure 4). For XBB.1 and XBB.1.5 complexes, we observed strong positive correlations among residues 395–475 (Figure 4A,B).

The movements of these RBD residues are anticorrelated with the displacements of the RBM tip (residues 475–487). This reflects a more stable RBD in the XBB.1.5 complex yielding strong dynamic couplings between the RBD core and more flexible regions of the binding interface. Hence, conformational dynamics of the XBB.1.5 RBD exhibited signs of long-range allosteric couplings between the RBD core elements and flexible loops that could collectively determine the RBD response to binding (Figure 4A,B). A different pattern of dynamic couplings was observed for BQ.1 (Figure 4C) and BQ.1.1 (Figure 4D). For BQ variants, positive dynamic correlations were seen for residues 335–375 and 396–455 in the RBD, while the movements of the flexible loop (residues 375–395) are anticorrelated with the RBD core. Common to XBB.1.5 and BQ.1.1 RBDs is the presence of negative cross-correlations between motions of the RBM tip (residues 475–487) and other RBD regions (residues 400–470 and 490–520) (Figure 4), where the extent of anticorrelation is stronger for the XBB.1.5 RBD (Figure 4B). The key differences in the conformational dynamics of the Omicron RBD-ACE2 complexes were further exemplified by the DCC maps showing the reduced mobility of the RBM loops in XBB.1.5 and BQ.1.1 and the enhanced long-range dynamic couplings between RBD regions in these complexes (Figure 4).

To conclude, microsecond MD simulations of the Omicron RBD-ACE2 complexes presented convincing evidence of distinct dynamic patterns in the otherwise structurally

similar Omicron RBD-ACE2 complexes. Consistent with the experimental data, our results showed that XBB.1.5 and BQ.1.1 mutations may induce the increased stabilization of the RBD, which may be linked with the experimentally observed greater RBD stability and enhanced ACE2 binding of the XBB.1.5 variant compared to the other variants.[55–57]

Dimensionality Reduction Analysis Unveils Differences in Conformational Heterogeneity of the Omicron RBD-ACE2 Complexes.

While the analysis of MD simulations and functional movements provided important insights into the underlying conformational landscape, the high dimensionality of the data sets produced by simulations often hinders salient dynamic signatures associated with the mechanisms of allosteric transitions. Here, to facilitate the conformational landscape analysis, we employed the tICA dimensionality reduction method to project the results of MD simulations into low-dimensional space.[105–108] The low-dimensionality projection of the MD ensemble in different microsecond trajectories highlighted a consistent occupancy of the dominant conformational region for the BA.2 complex (Figure 5A) as well as for the related XBB.1 (Figure 5B) and XBB.1.5 variants (Figure 5C). The dominant low-dimensional region is associated with "hook-like" folded conformation of the RBM tip, which is observed in the crystallographic conformations. Notably, this RBD conformation is also prevalent in the low-dimensional density distribution for the BA.4/BA.5 variant (Figure 5D). The conformational space of the BA.4/BA.5 variant (Figure 5D) remains narrow and similar to that of BA.2 (Figure 5A). In general, the commonly shared region in the low-dimensional space corresponds to the crystallographic conformations observed in the parental BA.2 and BA.4/BA.5 variants.

Nonetheless, in a striking contrast, a much larger conformational space is explored by the BQ.1 (Figure 5E) and BQ.1.1 variants (Figure 5F). This analysis showed that a small number of changes acquired in BQ.1 and BQ.1.1 variants due to accumulation of convergent mutations in R346, K444, L452, and N460 positions could lead to significant enhancement of the conformational variability and result in the noticeable redistribution in the population of conformational states (Figure 5E,F). The broader area of the conformational space for BQ.1 reflected the greater mobility of BQ.1 RBD (Figure 5E). Interestingly, the tICA projection of the conformational ensembles for the BQ.1.1 variant (Figure 5F) revealed some additional and unique regions of the conformational space compared to the closely related BQ.1 variant. The heterogeneity of the dynamic states revealed in the low-dimensional projection space for BQ.1 (Figure 5E) and BQ.1.1 (Figure 5F) suggested that convergent mutations may induce unique dynamic signatures of the conformational ensembles for these variants and promote the increased conformational plasticity of the RBD.

A common and powerful approach to probe conformational landscapes is to combine MD simulations with MSM analysis to estimate probabilities for protein transition among different macrostates. To build an effective MSM, it is important for a dimensionality reduction method to retain information about transitions among these macrostates. We analyzed the relaxation timescales in MSM, also referred to as implied timescales. The relaxation timescale can be interpreted as the time needed for a system to change its state.

In the tICA-reduced 2D space, the k-means clustering method was applied to partition the 2D data into 250 states. The implied timescales were calculated with lag times ranging from 0.1 to 12 ns. The top 15 timescales are shown (Figure 6A). The trend of the implied relaxation timescale revealed that the estimated timescale converged after about 5 ns, which was chosen as the lag time in the construction of MSM. Based on the gap of timescales, the number of macrostates was set to seven. The low-dimensional representation with 2 components (t-IC) showed some overlapping and the increased density of states in the dominant region sampled in all examined Omicron RBD-ACE2 systems (Figure 6B). These high-density regions are sampled in the BA.2, XBB.1, and XBB.1.5 variants (Figure 6B) and these regions are associated with macrostates 3 and 4 (Figure 6C). The less populated regions are sampled in the BQ.1 and BQ.1.1 variants where macrostates 1, 2, 5, 6, and 7 contribute to the overall distribution of states (Figure 6B,C). To visualize the distribution density of all simulations, a hexagon binning was employed where each hexagon represents a small region, and the color bar shows the frequency of this region (Figure 6D). The density plot revealed a clearly dominant area in the low-dimensional space sampled by all variants. Importantly this region is exclusively sampled by the XBB.1.5 variant, suggesting considerable stabilization of this complex. The least dense area of the distribution ("right leg") appeared mostly in a more dynamic BQ.1 variant. In general, the low-dimensional projection analysis emphasized the key differences in the conformational dynamics of the Omicron variants, where XBB.1 and XBB.1.5 RBDs tend to occupy a more limited area of the conformational space corresponding to the crystallographic conformation of the parental BA.2 variant. In contrast, convergent mutations in the BQ.1 and BQ.1.1 RBD complexes may induce greater conformational heterogeneity, which is particularly apparent in the BQ.1 variant with the most flexible RBD structure among studied systems.

After the partition of the MSM macrostates was determined (Supporting Materials, Figure S6), the stationary distribution and transition probabilities were calculated based on the constructed MSM. We determined the distributions of the Omicron RBD-ACE2 complexes in different macrostates which revealed the unique dynamic signatures and populations in each complex. The transition probabilities were determined among different macrostates for all systems, with the 5 ns lag time. The high percentage of self-conserved probability shows the stability of macrostates. We compared the distributions and transitional maps between parental BA.2 (Supporting Materials, Figure S7A) and XBB.1/XBB.1.5 subvariants (Figure 7A,B). For the BA.2 variant, we found that macrostates 3, 4, and 5 dominate the distribution with the macrostate 4 contributing ~51% to the conformational population (Supporting Materials, Figure S7A). The transitional map for BA.2 showed that the macrostates could have high kinetic barriers for transition to the other states (Supporting Materials Figure S7C). For example, for the macrostate 4, there is an overall probability of less than 0.5% to shift to two macrostates 3 and 5. At the same time, there is almost a 100% probability that minor macrostate 6 would interconvert to the macrostate 5 but close to zero probability of the reverse transition (Supporting Materials Figure S7B).

A comparative MSM analysis for XBB.1 and XBB.1.5 sublineages of BA.2 showed a reduction in the number of macrostates, where macrostates 3 and 4 dominate the conformational distribution for XBB.1 (Figure 7A,C) and XBB.1.5 RBDs (Figure 7B,D). Moreover, the population of macrostate 4 increased in the XBB.1.5 RBD to 86% from 75%

in the XBB.1 variant (Figure 7B). Structural analysis of the obtained macrostates showed that the differences between macrostates 3 and 4 are confined to the flexible RBM region (residues 470–491) that harbors several Omicron XBB.1/XBB.1.5 mutational sites and convergent Omicron sites F486P (F486S) and F490 (F490S) (Figure 8). The MSM analysis revealed that the dominant macrostate 4 featured well-ordered and stable "hook-like" RBM tip conformation. At the same time, macrostates 4 and 5 in BA.2 have a similar ordered RBM tip region but differ in the conformation of the flexible loop 440–452 (Figure 8). In macrostate 4, this loop assumes the crystallographic conformation of the BA.2 RBD, while this loop becomes more disordered in macrostate 5 (Figure 8). Hence, the major structural differences between major macrostates are mostly confined to the order–disorder transitions in the flexible loop regions 440–452 and 470–491. Interestingly, these regions harbor a number of convergent mutational sites including K444, V445, G446, N450, and L452 positions.

The transition maps for XBB.1 (Figure 7C) and XBB.1.5 (Figure 7D) unveiled a small transitional probability to interconvert from macrostate 4 to macrostate 5, indicating the increasing dominance of macrostate 4. The MSM analysis also revealed that dominant macrostate 4 featured well-ordered and stable "hook-like" conformation of the RBM tip centered on the F486P position in XBB.1.5 (Figure 8). This state becomes less favorable in XBB.1, while the contribution of macrostate 3 with a partly disordered conformation of the RBM tip increased. Based on the structural comparison of the macrostates, it becomes apparent that a combination of F486S and F490S mutations in XBB.1 may induce the increased mobility of the flexible RBM tip. On the other hand, the effect of F486P mutation in the XBB.1.5 variant can result in a partial restoration of the interfacial contacts mediated by F486P in this region. This analysis provides a plausible rationale of the experimental data which discovered that the XBB.1.5 variant is equally immune-evasive as XBB.1 but may have growth advantage due to the higher ACE2 binding. Deep mutational scanning experiments confirmed the effects of F486 mutations (F486V/I/S/L/A/P) showing that F486P imposes the lowest cost in RBD affinity loss and has the largest increase in RBD expression.[135,136] F486V (BA.4/BA.5), F486I, F486S (XBB.1), or F486P(XBB.1.5) also represents a convergent evolutionary hotspot shared by the Omicron subvariants and is one of the major hotspots for escaping neutralization by antibodies.[137]

A comparison of the macrostate distributions and transition maps for the parental BA.5 (Supporting Materials, Figure S7B,D) and BQ.1/BQ.1.1 variants (Figure 9) revealed a vastly different pattern even though the structures of all Omicron RBD-ACE2 complexes are similar. Interestingly, for the parental BA.5 variant, we observed populations of macrostate 3 and macrostate 1, where structurally macrostate 1 is more similar to the experimental structure and has a well-ordered RBM tip conformation (Supporting Materials, Figure S7B). Hence, the increased mobility of the BA.5 RBD is manifested in a more populated state with the very flexible RBM region (residues 470–491). Interestingly, the distribution is broadened in the BQ.1 variant showing significant contribution of macrostates 1 (34%), 2(11%), 3 (35%), and 7 (20%) (Figure 9A,C). Structural analysis showed that macrostates 3 and 7 are similar in their partly distorted RBM tip conformation but these macrostates are different in the conformation of the loop 440–452 (Figure 8). The macrostate 1 has a well-ordered RBM

tip but featured conformational differences distributed over the flexible loops in the RBD (Figure 8).

The transitional maps showed that macrostates 3, 1, and 4 tend to occupy neighboring areas of conformational space (Figure 9). Interestingly, the distribution of macrostates can be altered in the BQ.1 variant (Figure 9A,C), as macrostate 1 begins to dominate the population, while the contribution of macrostate 4 is markedly diminished. The transition map for BQ.1 showed that macrostate 4 can convert to macrostate 1 with 77% probability, while the reversed transition is highly unfavorable (Figure 9C,D). Macrostate 3 is also connected with macrostates 2 and 7 in the BQ.1 variant. The dominant population of macrostates for BQ.1 is characterized by distorted and partly disordered RBM tip conformation featured in macrostates 3 and 7 and enhanced flexibility of the RBD loops in macrostate 1.

Remarkably, the MSM analysis indicated that the distribution of macrostates can be markedly altered in the closely related BQ.1.1 variant (Figure 9B,D). We observed the population shift to macrostates 3, 4, and 6 dominating the conformational distribution with macrostate 4 contributing 43%, macrostate 3 contributing 33%, and macrostate 6 providing 22% of the total population (Figure 9B,D). While macrostate 3 has a partially disordered RBM tip, macrostate 6 displayed alterations in the flexible loop 440–452 compared to the crystallographic conformation of the BA.5 RBD (Figure 9B,D). The transition map showed that macrostate 5 could interconvert to macrostate 4 with ~17% probability, but the interconversion between states 4 and 3 is less probable (with only 3.9% from state 3 to 4 and 2.5% of the reversed transition) (Figure 9D). At the same time, macrostate 2 could readily interconvert to macrostate 3 with a 100% probability and macrostate 6 can convert to macrostate 5 with a 47% probability (Figure 9D).

Although the distribution of macrostates in BQ.1.1 becomes more similar to that of the XBB.1.5 variant, revealing the critical contribution of macrostates 3 and 4, the population of conformational states is significantly broader than that in XBB.1.5 (Figure 9C,D). In addition to the most dominant macrostate 4, the combined contributions of macrostates 3 and 6 are equally significant. These macrostates feature distinct variations of the flexible RBD loops 440–452 and 470–491 in the BQ.1.1 variant. As a result, the BQ.1.1 RBD may exist in a dynamic equilibrium between the crystallographic conformation seen in the parental BA.5 RBD and more dynamic states with highly variable RBM loops (Figure 9C,D). These results demonstrated that convergent mutations that are characteristic of the BQ.1 and BQ.1.1 variants could significantly change the dynamic equilibrium and modulate the increased flexibility of the RBD in these Omicron variants compared to a more stable RBD in the XBB.1.5 variant.

The MSM analysis provided a detailed characterization of conformational macrostates, revealing the unique and distinct dynamic signatures of structurally similar Omicron RBD-ACE2 complexes. One of key findings of this analysis revealed a strong preference of XBB.1.5 for a single macrostate associated with the ordered RBM conformation due to the restoration of F486P contacts with ACE2 inducing curtailed mobility in this region. Our results suggest that this dynamic signature may allow XBB.1.5 to maintain immune evasion

while protecting the RBD stability and binding. In contrast, the dominant macrostates in XBB.1 are characterized by highly flexible RBM conformation induced by F486S mutation and weaker ACE2 contacts which may explain the growth advantages of the XBB.1.5 variant. Another key finding is the emergence of several dominant macrostates in the BQ.1.1 variant including conformations with the highly flexible loop 440–452. Based on our results, BQ.1.1 variant mutations (R346T, K444T, and N460K) can increase the mobility in the loop harboring convergent mutational sites K444T, V445, and G446. Notably, BQ.1.1 bears all five recent convergent mutations: R346T, K444T, L452R, N460K, and F486V. The increased adaptability of the 440–452 loop may provide means for the enhanced immune evasion of the BQ.1.1 variant, further emphasizing the role of convergent mutations in modulating the flexibility of the mobile regions.

In general, MSM analysis consistently showed that major macrostates in the Omicron variants may differ due to variations in the intrinsically flexible RBD loops 470–491 and 440–452 involved in the interfacial contacts and containing sites of convergent mutations K444, V445, G446, N450, L452, and F486. Our results suggested that the variant-specific changes of conformational mobility in these functional loops may be modulated and altered through accumulation of various convergent mutations, thereby providing an evolutionary path for the improved immune escape without incurring a significant cost on the ACE2 binding. Moreover, the immune pressure on the RBD that promotes convergent evolution may be localized in these functional loops responsible for dynamic differences between variants. We argue that through this interplay of dynamic changes modulated by convergent mutations, BA.2/XBB.1/XBB.1.5 or BA.5/BQ.1/BQ.1.1 subvariants can enhance antibody escape.

Perturbation Response Scanning Reveals the Complementary Role of Convergent Mutations as Allosteric Effector and Sensor Centers.

Patterns of convergence are often offered as evidence of adaptation, and recent studies indicated that allosteric interactions in proteins can not only dictate long-range couplings and signal transmission patterns but are also essential in the evolutionary adaptation of proteins.[138,139] It has been recognized that allosteric mechanisms can regulate contribution of different conformational states and shape up functional landscapes in proteins, enabling evolutionary adaptation of new functions through controlled modulation of conformational plasticity.[139]

We hypothesized that sites of convergent mutations target specific structural hotspot of adaptation that may be organized through engagement to the pre-existing allosteric network. In this model, convergent mutations may work in concert with each other to potentiate functional protein adaptation to binding and immune escape via modulation of conformational flexibility in the key regions. According to the MSM analysis, we suggest that specific modulation of mobility in the two flexible regions (residues 440–452 and 470–491) may be orchestrated through the allosteric interaction network that couples sites convergent mutations.

To explore potential allosteric roles of the convergent mutations in RBD and characterize how Omicron variants can exploit these sites to optimize functional adaptation, we

employed perturbation profiling methodology to interrogate the inter-residue couplings and particularly probe the role of convergent mutations in mediating long-range allosteric effects in the Omicron RBD-ACE2 structures. The PRS method[118–120] was used to examine the allosteric roles of the RBD residues using the conformational ensembles of the XBB.1/XBB.1.5 and BQ.1/BQ.1.1 RBD-ACE2 complexes (Figure 10). The effector profiles measured the allosteric capacity of residue i to influence dynamics changes in all other residues, with the local maxima usually attributed to allosteric centers that may control propagation of perturbations over long distance and allosteric communications in the system. At the same time, the transmission capacity of residue j to perturbations can be evaluated from sensor distributions in which major peaks are often aligned with flexible regions experiencing large functional changes.

The PRS analysis revealed consistent effector peaks corresponding to sites with a high allosteric potential (residues 338–353, 400–406, 420–422, 432–436, 450–456, and 501–512) that are conserved across all RBD-ACE2 complexes (Figure 10A,B). The highest peaks corresponded to the hydrophobic RBD core (residues 399–402) and RBD segment (residues 505–512) that connects N501Y and Y505H interfacial positions with the central RBD core (Figure 10A,B). The major allosteric effector clusters were also observed in the functionally important segment (residues 450–456) harboring convergent mutational sites N450 and L452R and connecting the RBD core with the ACE2 binding interface (Figure 10A,B). We also found that the effector distribution peaks featured higher values for the XBB.1.5 (Figure 10A), suggesting that the structural stability of the RBD for this variant may further amplify the effect of the corresponding allosteric hotspots. Of particular interest was a comparison of the effector profiles for XBB.1.5 (Figure 10A) and BQ.1.1 variants (Figure 10B). The overall shape of the effector profiles and the distribution of major peaks were quite similar, indicating that the allosteric networks in both variants could be controlled through the same key RBD positions. By projecting positions of convergent mutational sites on the distributions, it can be seen that N450, L452R, R493Q, S494, and especially Y501 residues correspond to major allosteric centers that regulate long-range couplings (Figure 10A,B). There is a visible concentration of the effector sites near the critical interfacial region anchored by the Y501 position which is experimentally shown to be involved in short- and long-range epistatic relationships with other RBD sites.[64,65,136]

These sites could mediate an ensemble of well-defined signaling paths from the RBD core to the interface regions. Interestingly, by inspecting the effector potential for the entire spectrum of Omicron mutational sites in XBB.1.5 and BQ.1.1 variants, we noticed that many of other Omicron positions featured only moderate effector values. The sensor profiles were similar between XBB.1/XBB.1.5 and BQ.1/BQ.1.1 variants (Figure 10C,D) featuring convergent mutation sites N460K and F486S/V as important local peaks of the distribution. It is worth mentioning that highly flexible peripheral RBD regions displayed higher sensor peaks and could be involved in transmission of allosteric changes. We argue that these sensor clusters may allow the S-RBD to exploit conformational plasticity to mediate binding response to various classes of antibodies.

We also performed structure-based PRS analysis of major macrostates (Figure 11). Interestingly, significant differences were observed in both the effector and sensor profiles.

Consistent with the major contribution of macrostate 4 to the population of XBB.1/XBB.1.5 and BQ.1.1 states, the effector profile for this macrostate featured highest peaks (Figure 11A). Notably, a significant fraction of convergent mutation sites including N440K, K444T, V445P, G446S, N450, and L452R exhibited high effector potential values in macrostate 4. Moreover, the effector potential of these sites diminished in more dynamic macrostates 3 and 6 that contribute significantly to the population distribution of BQ.1 and BQ.1.1 variants (Figure 11A). Another cluster of notable effector centers is concentrated near R493Q, S494, and Y501 sites. On the other hand, highly flexible convergent mutation sites T478R/K, E484K and F486S/P are prominently featured among sensor hotspots of allosteric perturbations (Figure 11B). The sensor potential of these residues is amplified in macrostate 6 in which the flexibility of the loops 440–452 and 470–491 is redistributed and enhanced compared to macrostate 4. Hence, convergent mutations in the RBM regions may function as sensor hotspots of allosteric signals that is enabled through modulation of conformational plasticity in these regions.

Structural superposition of the major macrostates with the crystallographic conformations of BA.2 and BA.5 RBD showed overall fold similarity, while also highlighting differences in modulation of the flexible RBD loops (Figure 11C-E). Macrostate 3 displayed a distorted RBM conformation that abrogated "hook-like" folded arrangement of the RBM tip (Supporting Materials, Figure S8A). At the same time, macrostate 4 is similar to the crystallographic BA.2 and BA.5 conformations showing a close structural overlap in the loops 440–452 and 470–491 (Supporting Materials, Figure S8B). On the other hand, macrostate 6 featured a significant displacement of the loop 440–452 and moderate fluctuations of the RBM tip region (Supporting Materials, Figure S8C).

Collectively, these observations suggested that convergent mutation sites may play complementary roles in shaping up the long-range allosteric couplings and mediating changes in conformational plasticity of the RBD. Indeed, K444T, N450, L452R, and Y501 correspond to the effector centers of allosteric interactions and could control conformational changes in the flexible loop 440–452. The analysis revealed that convergent mutation sites, N460K, T478K, and F486/V/S/P of the mobile RBM tip (Supporting Materials, Figure S1) serve as major transmitters of long-range signals in the RBD-ACE2 complexes. According to the PRS analysis, the allosteric crosstalk between sites of convergent mutations acting as allosteric effectors and receivers may provide a mechanism for exerting such coordinated control among interfacial regions. Structural hotspots in adaptation often refer to specific regions or residues that have undergone significant changes or variations during the process of adaptation, which play a critical role in conferring new functions or improving existing functions in response to evolutionary pressures. The observed variations of conformational flexibility in the two flexible RBD loops 440–452 and 470–491 observed in the macrostates may be evolutionary beneficial for immune escape without compromising binding and stability. Combined, the results of MSM analysis and PRS modeling suggested that convergent mutations may be involved in long-range epistatic interactions where mutational changes in spatially distant communicating residues may control the extent of conformational plasticity in the flexible regions. According to our findings, convergent mutations may enable variant-specific adaptation of conformational dynamics in the interfacial regions and shape up conformational landscapes to control immune escape, while

preserving the RBD stability, functionality, and ACE2 binding. A potential implication of these results is that cumulative effects of individually near-neutral RBD mutations may allow for evolutionary adaptation and modulation of conformational mobility.[131] Although mutations in viruses occur randomly as the virus replicates where most of these mutations have no significant effect on the virus's characteristics, the emergence of Omicron mutations and a pattern of convergent mutations may confer the increased transmissibility and the ability to evade the immune system. These advantageous mutations can then become more prevalent in subsequent viral populations. Our findings are consistent with a mechanism in which Omicron mutations that achieved high transmissibility and antigenicity of the virus may promote a balance of the RBD folding stability and conformational adaptability to ensure the proper tradeoff between protein viability, binding to the host receptor and immune escape.

Inferring Evolution of Allosteric Cryptic Pockets from Conformational Ensembles and Macrostates.

The reversed allosteric communication approach is based on the premise that allosteric signaling in proteins is bidirectional and can propagate from an allosteric to orthosteric site and vice versa.[127,140–142] A more integrated computational and experimental strategy exploited the reversed allosteric communication concepts to combine MD simulations and MSM analysis to monitor shifts in the protein conformational ensembles and detect cryptic allosteric sites.[136,137] We have recently developed a fast and accurate allosteric site prediction method PASSer,[87] and here, this approach was employed for detection of allosteric RBD pockets using information about conformational ensembles and major functional macrostates of the Omicron RBD-ACE2 complexes. To simplify the presentation of the results, we focused on the predicted RBD pockets for the optimized structural models of XBB and BQ variants (Supporting Materials, Figures S9,S10) as well as on a detailed analysis of the determined cryptic pockets that are specific for each of the determined macrostates (Figure 12). The allosteric pockets predicted in the structural models of the XBB and BQ variants shared a conserved and experimentally determined allosteric site in the RBD core where the essential free fatty acid linoleic acid (LA) binds.[143] The cryo-EM structure of the SARS-CoV-2 S linoleic acid complex revealed this distal binding site and experimentally validated the allosteric effect of LA binding. The conserved allosteric pocket discovered experimentally is lined up by residues F338, V341, F342, F377, F374, F392, and W436. Our predicted pocket in this region is formed by residues F338, F342, Y369, F371, A372, I434, and W436 (Supporting Materials, Figures S9,S10). Notably, these residues also emerged as allosteric effector hotspots in the PRS analysis of allosteric communications in the Omicron complexes. In addition, the analysis also revealed that allosteric pockets may be formed near the RBM region (residues R454, F456, R457, K458, S469, E471, and I473) (Supporting Materials, Figures S9,S10). Interestingly, we also found that BQ.1 and BQ.1.1 RBD structures may open up allosteric pocket that is formed by functional sites near binding hotspot Y501 and convergent mutational hotspots L452R and S494. This pocket was detected only for these Omicron variants and is formed by RBD residues S494, Y495, R403, L452R, Y453, Y501, and G502 (Supporting Materials, Figure S10). Hence, we suggested that convergent mutational sites owing to evolutionary adaptability and conformational plasticity may be involved in modulation of opening/closing of cryptic allosteric sites.

To compare and validate the PASSer results in detection of allosteric pockets, we also examined macrostates and probed binding pockets using an alternative P2Rank/PrankWeb approach.[144,145] A considerable consistency in recovering the experimentally known allosteric site was seen when using both PASSer and PrankWeb approaches. The residue-based allosteric pocket propensities[139] for the RBD residues in seven major macrostates revealed the presence of a dense cluster in the RBD core associated with the experimentally known allosteric binding site (Figure 12A–C). This conserved pocket is also preserved in the conformational ensembles and is shared between all Omicron variants. In addition, we also discovered that the distribution peaks can be associated with the RBD regions near the binding hotspot Y501/H505 and strong contributions of convergent mutational sites K444, N450, and L452 (Figure 12A,B). These peaks are particularly strong in macrostates 3 and 4 that are highly prevalent in XBB.1/XBB.1.5 variants. While the composition of these pockets may change in the macrostates, these functional convergent mutations tend to orchestrate the formation and evolution of cryptic pockets in the conformational ensembles. Structural mapping showed evolution of the cryptic pockets in the RBD while also highlighting the preservation of the experimentally determined binding site (Figure 12D–F). The results show that variant-specific redistribution of macrostates preserves the experimentally known allosteric pocket on the RBD while allowing for the emergence of hidden allosteric pockets that are anchored by convergent mutation sites K444T and L452R In macrostate 3 with a disordered RBM tip, the allosteric pocket near the RBM region may "dissolve" providing a very plastic and "pocketless" interface in this region (Figure 12D). Similarly, macrostate 6 featuring altered and highly flexible loop 440–452 may induce stabilization of the RBD core pockets that occupy regions near the experimental allosteric site (Figure 12F).

Some of these pockets have a transient character and may emerge and disappear in different conformational states. In the dominant macrostate 4, we found several conserved pockets including the experimentally discovered allosteric site along with two adjacent small pockets and RBM pocket (Figure 12E). These allosteric binding sites are maintained in the dominant macrostate and could be targeted in both XBB and BQQ variants. One of the more interesting observations of the allosteric pocket analysis was detection of two additional pockets in macrostate 4 (shown in orange and yellow on Figure 12E) that are adjacent to the experimental allosteric site and contain a number of convergent mutation sites. In particular, one of these pockets (shown in yellow on Figure 12E) is formed by residues R346T, T347, N440K, L441, D442, K444, N448, N450, and L452. Strikingly, this allosteric pocket included several key convergent mutation sites (R346T, K444, N450, and L452) that also play a role as allosteric effector centers. Another pocket shown in orange in Figure 12E (residues R454, F456, R457, K458, D467, S469, E471, and I472) links the RBD core with the binding interface. Both these allosteric pockets are anchored by convergent mutation sites N450 and L452R. Hence, these hotspots could play an integrated role in modulating the conformational plasticity and viability of these pockets.

Together, these results showed that a selective group of convergent mutation sites could function as allosteric effector centers that control evolution and distribution of allosteric pockets through modulation of conformational plasticity in the flexible adaptable regions of the RBD. These findings indicated that Omicron XBB.1.5 and BQ.1.1 subvariants may

evolve to accumulate convergent mutations in flexible sites to modulate allostery and immune escape through opening/closing patches/pockets to control access of antibodies.

CONCLUSIONS

The new generation of SARS-CoV-2 Omicron variants displayed increased viral fitness by acquiring convergent mutations, suggesting that the immune pressure can promote convergent evolution. While evolutionary and functional studies explored various scenarios underlying the balance of virus fitness tradeoffs, a systematic analysis of the effects of convergent mutations on the conformational landscape of the RBD-ACE2 binding in newly emerged Omicron variants is lacking. In the current study, microsecond MD simulations and Markovian modeling characterized the conformational landscapes and functional states of the RBD-ACE2 complexes for the recently emerged highly transmissible XBB.1, XBB.1.5, BQ.1, and BQ.1.1 Omicron variants. Our results revealed the increased thermodynamic stabilization of the XBB.1.5 subvariant, while the flexibility of the RBD can be markedly increased in the BQ.1 and BQ.1.1 subvariants. Despite considerable structural similarities, Omicron mutations can induce unique dynamic signatures and specific distributions of conformational states in the Omicron variants. The results suggested that variant-specific changes of conformational mobility in the flexible RBD loops 470–491 and 440–452 can be modulated through allosteric couplings between convergent mutations, which may present a plausible mechanism for promoting the diverse immune escape without compromising the ACE2 binding. By combining MD simulations and MSM analysis with perturbation-based response profiling approaches, our study revealed important complementary roles of convergent mutation sites as effectors/regulators and sensors/receivers of allosteric signal transmission in the RBD-ACE2 complexes. The findings of this study suggested that convergent mutation sites may play important roles in shaping up the allosteric changes and mediating functional tradeoffs between protein stability, binding to the host receptor and immune escape. We also explored the reversed allosteric communication approach and characterized the effect of dynamics on the distribution of allosteric pockets in the Omicron subvariants. The results show that variant-specific redistribution of macrostates preserves the experimentally known allosteric RBD pocket while also revealing a spectrum of hidden allosteric pockets that are anchored by convergent mutation sites K444T and L452R. Through integrative computational approaches, this investigation provides a systematic analysis and comparison of the effects of Omicron subvariants on conformational dynamics and allosteric signaling in the complexes with the ACE2 receptor.

Supplementary Material

Refer to Web version on PubMed Central for supplementary material.

ACKNOWLEDGMENTS

Data Availability Statement

Data is fully contained within the article and Supporting Materials. Crystal structures were obtained and downloaded from the Protein Data Bank (http://www.rcsb.org). All simulations were performed using openMM high-performance toolkit for molecular simulation that was obtained from websites https://openmm.org/; https://simtk.org/projects/openmm and https://github.com/openmm/openmm. All simulations were performed using the all-atom additive CHARMM36M protein force field that can be obtained from http://mackerell.umaryland.edu/charmm_ff.shtml. The rendering of protein structures was done with the UCSF ChimeraX package (https://www.rbvi.ucsf.edu/chimerax/) and Pymol (https://pymol.org/2/). The software tools used in this study are freely available at GitHub sites https://github.com/smu-tao-group/protein-VAE and https://github.com/smu-tao-group/PASSer2.0. All of the data obtained in this work including simulation trajectories, topology and parameter files, the software tools, and the in-house scripts are freely available at DOI 10.5281/zenodo.7942171. Version 1 10.5281/zenodo.7942172.

REFERENCES

(1). Tai W; He L; Zhang X; Pu J; Voronin D; Jiang S; Zhou Y; Du L Characterization of the receptor-binding domain (RBD) of 2019 novel coronavirus: implication for development of RBD protein as a viral attachment inhibitor and vaccine. Cell. Mol Immunol 2020, 17, 613–620. [PubMed: 32203189]

(2). Wang Q; Zhang Y; Wu L; Niu S; Song C; Zhang Z; Lu G; Qiao C; Hu Y; Yuen KY; Wang Q; Zhou H; Yan J; Qi J Structural and functional basis of SARS-CoV-2 entry by using human ACE2. Cell 2020, 181, 894–904.e9. [PubMed: 32275855]

(3). Walls AC; Park YJ; Tortorici MA; Wall A; McGuire AT; Veesler D Structure, Function, and Antigenicity of the SARS-CoV-2 Spike Glycoprotein. Cell 2020, 181, 281–292.e6. [PubMed: 32155444]

(4). Wrapp D; Wang N; Corbett KS; Goldsmith JA; Hsieh CL; Abiona O; Graham BS; McLellan JS Cryo-EM structure of the 2019-nCoV spike in the prefusion conformation. Science 2020, 367, 1260–1263. [PubMed: 32075877]

(5). Cai Y; Zhang J; Xiao T; Peng H; Sterling SM; Walsh RM Jr; Rawson S; Rits-Volloch S; Chen B Distinct conformational states of SARS-CoV-2 spike protein. Science 2020, 369, 1586–1592. [PubMed: 32694201]

(6). Hsieh CL; Goldsmith JA; Schaub JM; DiVenere AM; Kuo HC; Javanmardi K; Le KC; Wrapp D; Lee AG; Liu Y; Chou CW; Byrne PO; Hjorth CK; Johnson NV; Ludes-Meyers J; Nguyen AW; Park J; Wang N; Amengor D; Lavinder JJ; Ippolito GC; Maynard JA; Finkelstein IJ; McLellan JS Structure-based design of prefusion-stabilized SARS-CoV-2 spikes. Science 2020, 369, 1501–1505. [PubMed: 32703906]

(7). Henderson R; Edwards RJ; Mansouri K; Janowska K; Stalls V; Gobeil SMC; Kopp M; Li D; Parks R; Hsu AL; Borgnia MJ; Haynes BF; Acharya P Controlling the SARS-CoV-2 spike glycoprotein conformation. Nat. Struct. Mol. Biol 2020, 27, 925–933. [PubMed: 32699321]

(8). McCallum M; Walls AC; Bowen JE; Corti D; Veesler D Structure-guided covalent stabilization of coronavirus spike glycoprotein trimers in the closed conformation. Nat. Struct. Mol. Biol 2020, 27, 942–949. [PubMed: 32753755]

(9). Xiong X; Qu K; Ciazynska KA; Hosmillo M; Carter AP; Ebrahimi S; Ke Z; Scheres SHW; Bergamaschi L; Grice GL; Zhang Y; CITIID-NIHR COVID-19 BioResource Collaboration;

Nathan JA; Baker S; James LC; Baxendale HE; Goodfellow I; Doffinger R; Briggs JAG. A thermostable, closed SARS-CoV-2 spike protein trimer. Nat. Struct. Mol. Biol 2020, 27, 934–941. [PubMed: 32737467]

(10). Costello SM; Shoemaker SR; Hobbs HT; Nguyen AW; Hsieh CL; Maynard JA; McLellan JS; Pak JE; Marqusee S The SARS-CoV-2 spike reversibly samples an open-trimer conformation exposing novel epitopes. Nat. Struct. Mol. Biol 2022, 29, 229–238. [PubMed: 35236990]

(11). McCormick KD; Jacobs JL; Mellors JW The emerging plasticity of SARS-CoV-2. Science 2021, 371, 1306–1308. [PubMed: 33766871]

(12). Ghimire D; Han Y; Lu M Structural Plasticity and Immune Evasion of SARS-CoV-2 Spike Variants. Viruses 2022, 14, 1255. [PubMed: 35746726]

(13). Xu C; Wang Y; Liu C; Zhang C; Han W; Hong X; Wang Y; Hong Q; Wang S; Zhao Q; Wang Y; Yang Y; Chen K; Zheng W; Kong L; Wang F; Zuo Q; Huang Z; Cong Y Conformational dynamics of SARS-CoV-2 trimeric spike glycoprotein in complex with receptor ACE2 revealed by cryo-EM. Sci. Adv 2021, 7, No. eabe5575.

(14). Benton DJ; Wrobel AG; Xu P; Roustan C; Martin SR; Rosenthal PB; Skehel JJ; Gamblin SJ Receptor binding and priming of the spike protein of SARS-CoV-2 for membrane fusion. Nature 2020, 588, 327–330. [PubMed: 32942285]

(15). Turoňová B; Sikora M; Schürmann C; Hagen WJH; Welsch S; Blanc FEC; von Bülow S; Gecht M; Bagola K; Hörner C; van Zandbergen G; Landry J; de Azevedo NTD; Mosalaganti S; Schwarz A; Covino R; Mühlebach MD; Hummer G; Krijnse Locker J; Beck M In situ structural analysis of SARS-CoV-2 spike reveals flexibility mediated by three hinges. Science 2020, 370, 203–208. [PubMed: 32817270]

(16). Lu M; Uchil PD; Li W; Zheng D; Terry DS; Gorman J; Shi W; Zhang B; Zhou T; Ding S; Gasser R; Prevost J; Beaudoin-Bussieres G; Anand SP; Laumaea A; Grover JR; Lihong L; Ho DD; Mascola JR; Finzi A; Kwong PD; Blanchard SC; Mothes W Real-time conformational dynamics of SARS-CoV-2 spikes on virus particles. Cell Host Microbe. 2020, 28, 880–891.e8. [PubMed: 33242391]

(17). Yang Z; Han Y; Ding S; Shi W; Zhou T; Finzi A; Kwong PD; Mothes W; Lu M SARS-CoV-2 Variants Increase Kinetic Stability of Open Spike Conformations as an Evolutionary Strategy. mBio 2022, 13, No. e0322721.

(18). Díaz-Salinas MA,; Li Q; Ejemel M; Yurkovetskiy L; Luban J; Shen K; Wang Y; Munro JB Conformational dynamics and allosteric modulation of the SARS-CoV-2 spike. eLife 2022, 11, No. e75433.

(19). Han P; Li L; Liu S; Wang Q; Zhang D; Xu Z; Han P; Li X; Li X; Peng Q; Peng Q; Su C; Su C; Huang B; Huang B; Li D; Li D; Zhang R; Zhang R; Tian M; Tian M; Fu L; Fu L; Gao Y; Gao Y; Zhao X; Zhao X; Liu K; Liu K; Qi J; Qi J; Gao GF; Gao GF; Wang P Receptor binding and complex structures of human ACE2 to spike RBD from omicron and delta SARS-CoV-2. Cell 2022, 185, 630–640. [PubMed: 35093192]

(20). Saville JW; Mannar D; Zhu X; Srivastava SS; Berezuk AM; Demers JP; Zhou S; Tuttle KS; Sekirov I; Kim A; Li W; Dimitrov DS; Subramaniam S Structural and biochemical rationale for enhanced spike protein fitness in delta and kappa SARS-CoV-2 variants. Nat. Commun 2022, 13, No. 742.

(21). Wang Y; Liu C; Zhang C; Wang Y; Hong Q; Xu S; Li Z; Yang Y; Huang Z; Cong Y Structural basis for SARS-CoV-2 Delta variant recognition of ACE2 receptor and broadly neutralizing antibodies. Nat. Commun 2022, 13, No. 871.

(22). Zhang J; Xiao T; Cai Y; Lavine CL; Peng H; Zhu H; Anand K; Tong P; Gautam A; Mayer ML; Walsh RM Jr; Rits-Volloch S; Wesemann DR; Yang W; Seaman MS; Lu J; Chen B Membrane fusion and immune evasion by the spike protein of SARS-CoV-2 Delta variant. Science 2021, 374, 1353–1360. [PubMed: 34698504]

(23). Mannar D; Saville JW; Zhu X; Srivastava SS; Berezuk AM; Tuttle KS; Marquez AC; Sekirov I; Subramaniam S SARS-CoV-2 Omicron variant: Antibody evasion and cryo-EM structure of spike protein-ACE2 complex. Science 2022, 375, 760–764. [PubMed: 35050643]

(24). Hong Q; Han W; Li J; Xu S; Wang Y; Xu C; Li Z; Wang Y; Zhang C; Huang Z; Cong Y Molecular basis of receptor binding and antibody neutralization of Omicron. Nature 2022, 604, 546–552. [PubMed: 35228716]

(25). McCallum M; Czudnochowski N; Rosen LE; Zepeda SK; Bowen JE; Walls AC; Hauser K; Joshi A; Stewart C; Dillen JR; Powell AE; Croll TI; Nix J; Virgin HW; Corti D; Snell G; Veesler D Structural basis of SARS-CoV-2 Omicron immune evasion and receptor engagement. Science 2022, 375, 864–868. [PubMed: 35076256]

(26). Yin W; Xu Y; Xu P; Cao X; Wu C; Gu C; He X; Wang X ; Huang S; Yuan Q; Wu K; Hu W; Huang Z; Liu J; Wang Z; Jia F; Xia K; Liu P; Wang X; Song B; Zheng J; Jiang H; Cheng X; Jiang Y; Deng SJ; Xu HE Structures of the Omicron Spike trimer with ACE2 and an anti-Omicron antibody. Science 2022, 375, 1048–1053. [PubMed: 35133176]

(27). Gobeil SM-C; Henderson R; Stalls V; Janowska K; Huang X; May A; Speakman M; Beaudoin E; Manne K; Li D; Parks R; Barr M; Deyton M; Martin M; Mansouri K; Edwards RJ; Eaton A; Montefiori DC; Sempowski GD; Saunders KO; Wiehe K; Williams W; Korber B; Haynes BF; Acharya P Structural Diversity of the SARS-CoV-2 Omicron Spike. Mol. Cell 2022, 82, 2050–2068.e6. [PubMed: 35447081]

(28). Cui Z; Liu P; Wang N; Wang L; Fan K; Zhu Q; Wang K; Chen R; Feng R; Jia Z; Yang M; Xu G; Zhu B; Fu W; Chu T; Feng L; Wang Y; Pei X; Yang P; Xie XS; Cao L; Cao Y; Wang X Structural and functional characterizations of infectivity and immune evasion of SARS-CoV-2 Omicron. Cell 2022, 185, 860–871.e13. [PubMed: 35120603]

(29). Zhou T; Wang L; Misasi J; Pegu A; Zhang Y; Harris DR; Olia AS; Talana CA; Yang ES; Chen M; Choe M; Shi W; Teng IT; Creanga A; Jenkins C; Leung K; Liu T; Stancofski ED; Stephens T; Zhang B; Tsybovsky Y; Graham BS; Mascola JR; Sullivan NJ; Kwong PD Structural basis for potent antibody neutralization of SARS-CoV-2 variants including B.1.1.529. Science 2022, 376, No. eabn8897.

(30). Guo H; Gao Y; Li T; Li T; Lu Y; Zheng L; Liu Y; Yang T; Luo F; Song S; Wang W; Yang X; Nguyen HC; Zhang H; Huang A; Jin A; Yang H; Rao Z; Ji X Structures of Omicron Spike Complexes and Implications for Neutralizing Antibody Development. Cell Rep. 2022, 39, No. 110770.

(31). Stalls V; Lindenberger J; Gobeil SM-C; Henderson R; Parks R; Barr M; Deyton M; Martin M; Janowska K; Huang X; May A; Speakman M; Beaudoin E; Kraft B; Lu X; Edwards RJ; Eaton A; Montefiori DC; Williams WB; Saunders KO; Wiehe K; Haynes BF; Acharya P Cryo-EM Structures of SARS-CoV-2 Omicron BA.2 Spike. Cell Rep. 2022, 39, No. 111009.

(32). Lin S; Chen Z; Zhang X; Wen A; Yuan X; Yu C; Yang J; He B; Cao Y; Lu G Characterization of SARS-CoV-2 Omicron Spike RBD Reveals Significantly Decreased Stability, Severe Evasion of Neutralizing-Antibody Recognition but Unaffected Engagement by Decoy ACE2 Modified for Enhanced RBD Binding. Signal Transduct. Target Ther 2022, 7, No. 56.

(33). Zhao Z; Zhou J; Tian M; Huang M; Liu S; Xie Y; Han P; Bai C; Han P; Zheng A; Fu L; Gao Y; Peng Q; Li Y; Chai Y; Zhang Z; Zhao X; Song H; Qi J; Wang Q; Wang P; Gao GF Omicron SARS-CoV-2 Mutations Stabilize Spike up-RBD Conformation and Lead to a Non-RBM-Binding Monoclonal Antibody Escape. Nat. Commun 2022, 13, No. 4958.

(34). Cerutti G; Guo Y; Liu L; Liu L; Zhang Z; Luo Y; Huang Y; Wang HH; Ho DD; Sheng Z; Shapiro L Cryo-EM Structure of the SARS-CoV-2 Omicron Spike. Cell Rep. 2022, 38, No. 110428.

(35). Ye G; Liu B; Li F Cryo-EM Structure of a SARS-CoV-2 Omicron Spike Protein Ectodomain. Nat. Commun 2022, 13, No. 1214.

(36). Dejnirattisai W; Huo J; Zhou D; Zahradník J; Supasa P; Liu C; Duyvesteyn HME; Ginn HM; Mentzer AJ; Tuekprakhon A; Nutalai R; Wang B; Dijokaite A; Khan S; Avinoam O; Bahar M; Skelly D; Adele S; Johnson SA; Amini A; Ritter TG; Mason C; Dold C; Pan D; Assadi S; Bellass A; Omo-Dare N; Koeckerling D; Flaxman A; Jenkin D; Aley PK; Voysey M; Costa Clemens SA; Naveca FG; Nascimento V; Nascimento F; Fernandes da Costa C; Resende PC; Pauvolid-Correa A; Siqueira MM; Baillie V; Serafin N; Kwatra G; Da Silva K; Madhi SA; Nunes MC; Malik T; Openshaw PJM; Baillie JK; Semple MG; Townsend AR; Huang KA; Tan TK; Carroll MW; Klenerman P; Barnes E; Dunachie SJ; Constantinides B; Webster H; Crook D; Pollard AJ; Lambe T; Paterson NG; Williams MA; Hall DR; Fry EE; Mongkolsapaya J; Ren J; Schreiber G; Stuart DI; Screaton GR; et al. SARS-CoV-2 Omicron-B.1.1.529 leads to widespread escape from neutralizing antibody responses. Cell 2022, 185, 467–484.e415. [PubMed: 35081335]

(37). Cameroni E; Bowen JE; Rosen LE; Saliba C; Zepeda SK; Culap K; Pinto D; VanBlargan LA; De Marco A; di Iulio J; Zatta F; Kaiser H; Noack J; Farhat N; Czudnochowski N; Havenar-Daughton

C; Sprouse KR; Dillen JR; Powell AE; Chen A; Maher C; Yin L; Sun D; Soriaga L; Bassi J; Silacci-Fregni C; Gustafsson C; Franko NM; Logue J; Iqbal NT; Mazzitelli I; Geffner J; Grifantini R; Chu H; Gori A; Riva A; Giannini O; Ceschi A; Ferrari P; Cippà PE; Franzetti-Pellanda A; Garzoni C; Halfmann PJ; Kawaoka Y; Hebner C; Purcell LA; Piccoli L; Pizzuto MS; Walls AC; Diamond MS; Telenti A; Virgin HW; Lanzavecchia A; Snell G; Veesler D; Corti D Broadly neutralizing antibodies overcome SARS-CoV-2 Omicron antigenic shift. Nature 2022, 602, 664–670. [PubMed: 35016195]

(38). Barton MI; MacGowan SA; Kutuzov MA; Dushek O; Barton GJ; van der Merwe PA Effects of common mutations in the SARS-CoV-2 Spike RBD and its ligand, the human ACE2 receptor on binding affinity and kinetics. eLife 2021, 10, No. e70658.

(39). Cao Y; Wang J; Jian F; Xiao T; Song W; Yisimayi A; Huang W; Li Q; Wang P; An R; Wang J; Wang Y; Niu X; Yang S; Liang H; Sun H; Li T; Yu Y; Cui Q; Liu S; Yang X; Du S; Zhang Z; Hao X; Shao F; Jin R; Wang X; Xiao J; Wang Y; Xie XS Omicron escapes the majority of existing SARS-CoV-2 neutralizing antibodies. Nature 2022, 602, 657–663. [PubMed: 35016194]

(40). Liu L; Iketani S; Guo Y; Chan JF; Wang M; Liu L; Luo Y; Chu H; Huang Y; Nair MS; Yu J; Chik KK; Yuen TT; Yoon C; To KK; Chen H; Yin MT; Sobieszczyk ME; Huang Y; Wang HH; Sheng Z; Yuen KY; Ho DD Striking antibody evasion manifested by the Omicron variant of SARS-CoV-2. Nature 2022, 602, 676–681. [PubMed: 35016198]

(41). Zhang J; Cai Y; Lavine CL; Peng H; Zhu H; Anand K; Tong P; Gautam A; Mayer ML; Rits-Volloch S; Wang S; Sliz P; Wesemann DR; Yang W; Seaman MS; Lu J; Xiao T; Chen B Structural and functional impact by SARS-CoV-2 Omicron spike mutations. Cell Rep. 2022, 39, No. 110729.

(42). Li L; Liao H; Meng Y; Li W; Han P; Liu K; Wang Q; Li D; Zhang Y; Wang L; Fan Z; Zhang Y; Wang Q; Zhao X; Sun Y; Huang N; Qi J; Gao GF Structural basis of human ACE2 higher binding affinity to currently circulating Omicron SARS-CoV-2 sub-variants BA.2 and BA.1.1. Cell 2022, 185, 2952–2960.e10. [PubMed: 35809570]

(43). Xu Y; Wu C; Cao X; Gu C; Liu H; Jiang M; Wang X; Yuan Q; Wu K; Liu J; Wang D; He X; Wang X; Deng SJ; Xu HE; Yin W Structural and biochemical mechanism for increased infectivity and immune evasion of Omicron BA.2 variant compared to BA.1 and their possible mouse origins. Cell Res. 2022, 32, 609–620. [PubMed: 35641567]

(44). Tuekprakhon A; Nutalai R; Dijokaite-Guraliuc A; Zhou D; Ginn HM; Selvaraj M; Liu C; Mentzer AJ; Supasa P; Duyvesteyn HME; Das R; Skelly D; Ritter TG; Amini A; Bibi S; Adele S; Johnson SA; Constantinides B; Webster H; Temperton N; Klenerman P; Barnes E; Dunachie SJ; Crook D; Pollard AJ; Lambe T; Goulder P; Paterson NG; Williams MA; Hall DR; OPTIC Consortium; ISARIC4C Consortium; Fry EE; Huo J; Mongkolsapaya J; Ren J; Stuart DI; Screaton GR Antibody escape of SARS-CoV-2 Omicron BA.4 and BA.5 from vaccine and BA.1 serum. Cell 2022, 185, 2422–2433.e13. [PubMed: 35772405]

(45). Cao Y; Yisimayi A; Jian F; Song W; Xiao T; Wang L; Du S; Wang J; Li Q; Chen X; Yu Y; Wang P; Zhang Z; Liu P; An R; Hao X; Wang Y; Wang J; Feng R; Sun H; Zhao L; Zhang W; Zhao D; Zheng J; Yu L; Li C; Zhang N; Wang R; Niu X; Yang S; Song X; Chai Y; Hu Y; Shi Y; Zheng L; Li Z; Gu Q; Shao F; Huang W; Jin R; Shen Z; Wang Y; Wang X; Xiao J; Xie XS BA.2.12.1, BA.4 and BA.5 escape antibodies elicited by Omicron infection. Nature 2022, 608, 593–602. [PubMed: 35714668]

(46). Bowen JE; Addetia A; Dang HV; Stewart C; Brown JT; Sharkey WK; Sprouse KR; Walls AC; Mazzitelli IG; Logue JK; Franko NM; Czudnochowski N; Powell AE; Dellota E Jr; Ahmed K; Ansari AS; Cameroni E; Gori A; Bandera A; Posavad CM; Dan JM; Zhang Z; Weiskopf D; Sette A; Crotty S; Iqbal NT; Corti D; Geffner J; Snell G; Grifantini R; Chu HY; Veesler D Omicron spike function and neutralizing activity elicited by a comprehensive panel of vaccines. Science 2022, 377, 890–894. [PubMed: 35857529]

(47). Huo J; Dijokaite-Guraliuc A; Liu C; Zhou D; Ginn HM; Das R; Supasa P; Selvaraj M; Nutalai R; Tuekprakhon A; Duyvesteyn HME; Mentzer AJ; Skelly D; Ritter TG; Amini A; Bibi S; Adele S; Johnson SA; Paterson NG; Williams MA; Hall DR; Plowright M; Newman TAH; Hornsby H; de Silva TI; Temperton N; Klenerman P; Barnes E; Dunachie SJ; Pollard AJ; Lambe T; Goulder P; Fry EE; Mongkolsapaya J; Ren J; Stuart DI; Screaton GR A Delicate Balance between Antibody Evasion and ACE2 Affinity for Omicron BA.2.75. Cell Rep. 2023, 42, No. 111903.

(48). Cao Y; Song W; Wang L; Liu P; Yue C; Jian F; Yu Y; Yisimayi A; Wang P; Wang Y; Zhu Q; Deng J; Fu W; Yu L; Zhang N; Wang J; Xiao T; An R; Wang J; Liu L; Yang S; Niu X; Gu Q; Shao F; Hao X; Meng B; Gupta RK; Jin R; Wang Y; Xie XS; Wang X Characterization of the Enhanced Infectivity and Antibody Evasion of Omicron BA.2.75. Cell Host Microbe 2022, 30, 1527–1539.e5. [PubMed: 36270286]

(49). Callaway E. Coronavirus variant XBB.1.5 rises in the United States - is it a global threat? Nature 2023, 613, 222–223. [PubMed: 36624320]

(50). Parums DV Editorial: The XBB.1.5 ('Kraken') Subvariant of Omicron SARS-CoV-2 and its Rapid Global Spread. Med. Sci. Monit 2023, 29, No. e939580.

(51). Saito A; Tamura T; Zahradnik J; Deguchi S; Tabata K; Anraku Y; Kimura I; Ito J; Yamasoba D; Nasser H; Toyoda M; Nagata K; Uriu K; Kosugi Y; Fujita S; Shofa M; Monira Begum M; Shimizu R; Oda Y; Suzuki R; Ito H; Nao N; Wang L; Tsuda M; Yoshimatsu K; Kuramochi J; Kita S; Sasaki-Tabata K; Fukuhara H; Maenaka K; Yamamoto Y; Nagamoto T; Asakura H; Nagashima M; Sadamasu K; Yoshimura K; Ueno T; Schreiber G; Takaori-Kondo A; Shirakawa K; Sawa H; Irie T; Hashiguchi T; Takayama K; Matsuno K; Tanaka S; Ikeda T; Fukuhara T; Sato K Virological Characteristics of the SARS-CoV-2 Omicron BA.2.75 Variant. Cell Host Microbe 2022, 30, 1540–1555.e15. [PubMed: 36272413]

(52). Kimura I; Yamasoba D; Tamura T; Nao N; Suzuki T; Oda Y; Mitoma S; Ito J; Nasser H; Zahradnik J; Uriu K; Fujita S ; Kosugi Y; Wang L; Tsuda M; Kishimoto M; Ito H; Suzuki R; Shimizu R; Begum MM; Yoshimatsu K; Kimura KT; Sasaki J; Sasaki-Tabata K; Yamamoto Y; Nagamoto T; Kanamune J; Kobiyama K; Asakura H; Nagashima M; Sadamasu K; Yoshimura K; Shirakawa K; Takaori-Kondo A; Kuramochi J; Schreiber G; Ishii KJ; Hashiguchi T; Ikeda T; Saito A; Fukuhara T; Tanaka S; Matsuno K; Sato K Virological Characteristics of the SARS-CoV-2 Omicron BA.2 Subvariants, Including BA.4 and BA.5. Cell 2022, 185, 3992–4007.e16. [PubMed: 36198317]

(53). Tamura T; Ito J; Uriu K; Zahradnik J; Kida I; Anraku Y; Nasser H; Shofa M; Oda Y; Lytras S; Nao N; Itakura Y; Deguchi S; Suzuki R; Wang L; Begum MM; Kita S; Yajima H; Sasaki J; Sasaki-Tabata K; Shimizu R; Tsuda M; Kosugi Y; Fujita S; Pan L; Sauter D; Yoshimatsu K; Suzuki S; Asakura H; Nagashima M; Sadamasu K; Yoshimura K; Yamamoto Y; Nagamoto T; Schreiber G; Maenaka K; Ito H; Misawa N; Kimura I; Suganami M; Chiba M; Yoshimura R; Yasuda K; Iida K; Ohsumi N; Strange AP; Takahashi O; Ichihara K; Shibatani Y; Nishiuchi T; Kato M; Ferdous Z; Mouri H; Shishido K; Sawa H; Hashimoto R; Watanabe Y; Sakamoto A; Yasuhara N; Suzuki T; Kimura K; Nakajima Y; Nakagawa S; Wu J; Shirakawa K; Takaori-Kondo A; Nagata K; Kazuma Y; Nomura R; Horisawa Y; Tashiro Y; Kawai Y; Irie T; Kawabata R; Motozono C; Toyoda M; Ueno T; Hashiguchi T; Ikeda T; Fukuhara T; Saito A; Tanaka S; Matsuno K; Takayama K; Sato K Virological Characteristics of the SARS-CoV-2 XBB Variant Derived from Recombination of Two Omicron Subvariants. Nat. Commun 2023, 14, No. 2800.

(54). Wang Q; Iketani S; Li Z; Liu L; Guo Y; Huang Y; Bowen AD; Liu M; Wang M; Yu J; Valdez R; Lauring AS; Sheng Z; Wang HH; Gordon A; Liu L; Ho DD Alarming Antibody Evasion Properties of Rising SARS-CoV-2 BQ and XBB Subvariants. Cell 2023, 186, 279–286.e8. [PubMed: 36580913]

(55). Yue C; Song W; Wang L; Jian F; Chen X; Gao F; Shen Z; Wang Y; Wang X; Cao Y ACE2 Binding and Antibody Evasion in Enhanced Transmissibility of XBB.1.5. Lancet Infect. Dis 2023, 23, 278–280. [PubMed: 36746173]

(56). Lasrado N; Collier AY; Miller J; Hachmann NP; Liu J; Sciacca M; Wu C; Anand T; Bondzie EA; Fisher JL; Mazurek CR; Patio RC; Powers O; Rodrigues SL; Rowe M; Surve N; Ty DM; Korber B; Barouch DH Waning Immunity Against XBB.1.5 Following Bivalent mRNA Boosters. BioRxiv 2023, DOI: 10.1101/2023.01.22.525079.

(57). Uraki R; Ito M; Kiso M; Yamayoshi S; Iwatsuki-Horimoto K; Furusawa Y; Sakai-Tagawa Y; Imai M; Koga M; Yamamoto S; Adachi E; Saito M; Tsutsumi T; Otani A; Kikuchi T; Yotsuyanagi H; Halfmann PJ; Pekosz A; Kawaoka Y Antiviral and Bivalent Vaccine Efficacy against an Omicron XBB.1.5 Isolate. Lancet Infect. Dis 2023, 23, 402–403. [PubMed: 36773622]

(58). Yamasoba D; Uriu K; Plianchaisuk A; Kosugi Y; Pan L; Zahradnik J; Ito J; Sato K Virological Characteristics of the SARS-CoV-2 Omicron XBB.1.16 Variant. Lancet Infect Dis. 2023, 23, 655–656. [PubMed: 37148902]

(59). Focosi D; Quiroga R; McConnell S; Johnson MC; Casadevall A Convergent Evolution in SARS-CoV-2 Spike Creates a Variant Soup from Which New COVID-19 Waves Emerge. Int. J. Mol. Sci 2023, 24, 2264. [PubMed: 36768588]

(60). Ito J; Suzuki R; Uriu K; Itakura Y; Zahradnik J; Kimura KT; Deguchi S; Wang L; Lytras S; Tamura T; Kida I; Nasser H; Shofa M; Begum MM; Tsuda M; Oda Y; Suzuki T; Sasaki J; Sasaki-Tabata K; Fujita S; Yoshimatsu K; Ito H; Nao N; Asakura H; Nagashima M; Sadamasu K; Yoshimura K; Yamamoto Y; Nagamoto T; Kuramochi J; Schreiber G; Suzuki S; Kato M; Ferdous Z; Mouri H; Shishido K; Misawa N; Kimura I; Kosugi Y; Lin P; Suganami M; Chiba M; Yoshimura R; Yasuda K; Iida K; Ohsumi N; Strange AP; Sauter D; Nakagawa S; Wu J; Watanabe Y; Sakamoto A; Yasuhara N; Nakajima Y; Yajima H; Shirakawa K; Takaori-Kondo A; Nagata K; Kazuma Y; Nomura R; Horisawa Y; Tashiro Y; Kawa Y; Irie T; Kawabata R; Shimizu R; Takahashi O; Ichihara K; Motozono C; Toyoda M; Ueno T; Shibatani Y; Nishiuchi T; Saito A; Matsuno K; Takayama K; Hashiguchi T; Tanaka S; Fukuhara T; Ikeda T; Sato K Convergent Evolution of SARS-CoV-2 Omicron Subvariants Leading to the Emergence of BQ.1.1 Variant. Nat. Commun 2023, 14, No. 2671.

(61). Zhu A; Wei P; Man M; Liu X; Ji T; Chen J; Chen C; Huo J; Wang Y; Zhao J Antigenic Characterization of SARS-CoV-2 Omicron Subvariants XBB.1.5, BQ.1, BQ.1.1, BF.7 and BA.2.75.2. Signal Transduct. Target Ther 2023, 8, 125. [PubMed: 36922506]

(62). Planas D; Bruel T; Staropoli I; Guivel-Benhassine F; Porrot F; Maes P; Grzelak L; Prot M; Mougari S; Planchais C; Puech J; Saliba M; Sahraoui R; Fémy F; Morel N; Dufloo J; Sanjuán R; Mouquet H; André E; Hocqueloux L; Simon-Loriere E; Veyer D; Prazuck T; Péré H; Schwartz O Resistance of Omicron Subvariants BA.2.75.2, BA.4.6, and BQ.1.1 to Neutralizing Antibodies. Nat. Commun 2023, 14, No. 824.

(63). Zahradník J; Nunvar J; Schreiber G Perspectives: SARS-CoV-2 Spike Convergent Evolution as a Guide to Explore Adaptive Advantage. Front. Cell Infect. Microbiol 2022, 12, No. 748948.

(64). Starr TN; Greaney AJ; Hannon WW; Loes AN; Hauser K; Dillen JR; Ferri E; Farrell AG; Dadonaite B; McCallum M; Matreyek KA; Corti D; Veesler D; Snell G; Bloom JD Shifting mutational constraints in the SARS-CoV-2 receptor-binding domain during viral evolution. Science 2022, 377, 420–424. [PubMed: 35762884]

(65). Moulana A; Dupic T; Phillips AM; Chang J; Nieves S; Roffler AA; Greaney AJ; Starr TN; Bloom JD; Desai MM Compensatory Epistasis Maintains ACE2 Affinity in SARS-CoV-2 Omicron BA.1. Nat Commun. 2022, 13, No. 7011.

(66). Cao Y; Jian F; Wang J; Yu Y; Song W; Yisimayi A; Wang J; An R; Chen X; Zhang N; Wang Y; Wang P; Zhao L; Sun H; Yu L; Yang S; Niu X; Xiao T; Gu Q; Shao F; Hao X; Xu Y; Jin R; Shen Z; Wang Y; Xie XS Imprinted SARS-CoV-2 Humoral Immunity Induces Convergent Omicron RBD Evolution. Nature 2023, 614, 521–529. [PubMed: 36535326]

(67). Sztain T; Ahn SH; Bogetti AT; Casalino L; Goldsmith JA; Seitz E; McCool RS; Kearns FL; Acosta-Reyes F; Maji S; Mashayekhi G; McCammon JA; Ourmazd A; Frank J; McLellan JS; Chong LT; Amaro RE A glycan gate controls the opening of the SARS-CoV-2 spike protein. Nat. Chem 2021, 13, 963–968. [PubMed: 34413500]

(68). Sikora M; von Bülow S; Blanc FEC; Gecht M; Covino R; Hummer G Computational epitope map of SARS-CoV-2 spike protein. PLoS Comput. Biol. 2021, 17, No. e1008790.

(69). Pang YT; Acharya A; Lynch DL; Pavlova A; Gumbart JC SARS-CoV-2 Spike Opening Dynamics and Energetics Reveal the Individual Roles of Glycans and Their Collective Impact. Commun. Biol 2022, 5, No. 1170.

(70). Mori T; Jung J; Kobayashi C; Dokainish HM; Re S; Sugita Y Elucidation of interactions regulating conformational stability and dynamics of SARS-CoV-2 S-protein. Biophys. J 2021, 120, 1060–1071. [PubMed: 33484712]

(71). Zimmerman MI; Porter JR; Ward MD; Singh S; Vithani N; Meller A; Mallimadugula UL; Kuhn CE; Borowsky JH; Wiewiora RP; Hurley MFD; Harbison AM; Fogarty CA; Coffland JE; Fadda E; Voelz VA; Chodera JD; Bowman GR SARS-CoV-2 simulations go exascale to predict dramatic spike opening and cryptic pockets across the proteome. Nat. Chem 2021, 13, 651–659. [PubMed: 34031561]

(72). Mori T; Jung J; Kobayashi C; Dokainish HM; Re S; Sugita Y Elucidation of Interactions Regulating Conformational Stability and Dynamics of SARS-CoV-2 S-Protein. Biophys J. 2021, 120, 1060–1071. [PubMed: 33484712]

(73). Dokainish HM; Re S; Mori T; Kobayashi C; Jung J; Sugita Y The inherent flexibility of receptor binding domains in SARS-CoV-2 spike protein. eLife 2022, 11, No. e75720.

(74). Zuzic L; Samsudin F; Shivgan AT; Raghuvamsi PV; Marzinek JK; Boags A; Pedebos C; Tulsian NK; Warwicker J; MacAry P; Crispin M; Khalid S; Anand GS; Bond PJ Uncovering Cryptic Pockets in the SARS-CoV-2 Spike Glycoprotein. Structure 2022, 30, 1062–1074.e4. [PubMed: 35660160]

(75). Verkhivker GM Coevolution, dynamics and allostery conspire in shaping cooperative binding and signal transmission of the SARS-CoV-2 spike protein with human angiotensin-converting enzyme 2. Int. J. Mol. Sci 2020, 21, 8268. [PubMed: 33158276]

(76). Verkhivker GM Molecular simulations and network modeling reveal an allosteric signaling in the SARS-CoV-2 spike proteins. J. Proteome Res 2020, 19, 4587–4608. [PubMed: 33006900]

(77). Verkhivker GM; Di Paola L Dynamic Network Modeling of Allosteric Interactions and Communication Pathways in the SARS-CoV-2 Spike Trimer Mutants: Differential Modulation of Conformational Landscapes and Signal Transmission via Cascades of Regulatory Switches. J. Phys. Chem. B 2021, 125, 850–873. [PubMed: 33448856]

(78). Verkhivker GM; Di Paola L Integrated Biophysical Modeling of the SARS-CoV-2 Spike Protein Binding and Allosteric Interactions with Antibodies. J. Phys. Chem. B 2021,125, 4596–4619. [PubMed: 33929853]

(79). Verkhivker GM; Agajanian S; Oztas DY; Gupta G Comparative Perturbation-Based Modeling of the SARS-CoV-2 Spike Protein Binding with Host Receptor and Neutralizing Antibodies: Structurally Adaptable Allosteric Communication Hotspots Define Spike Sites Targeted by Global Circulating Mutations. Biochemistry 2021, 60, 1459–1484. [PubMed: 33900725]

(80). Verkhivker GM; Agajanian S; Oztas DY; Gupta G Dynamic Profiling of Binding and Allosteric Propensities of the SARS-CoV-2 Spike Protein with Different Classes of Antibodies: Mutational and Perturbation-Based Scanning Reveals the Allosteric Duality of Functionally Adaptable Hotspots. J. Chem. Theory Comput 2021, 17, 4578–4598. [PubMed: 34138559]

(81). Verkhivker GM; Agajanian S; Oztas DY; Gupta G Allosteric Control of Structural Mimicry and Mutational Escape in the SARS-CoV-2 Spike Protein Complexes with the ACE2 Decoys and Miniprotein Inhibitors: A Network-Based Approach for Mutational Profiling of Binding and Signaling. J. Chem. Inf. Model 2021, 61, 5172–5191. [PubMed: 34551245]

(82). Verkhivker G; Alshahrani M; Gupta G Coarse-Grained Molecular Simulations and Ensemble-Based Mutational Profiling of Protein Stability in the Different Functional Forms of the SARS-CoV-2 Spike Trimers: Balancing Stability and Adaptability in BA.1, BA.2 and BA.2.75 Variants. Int. J. Mol. Sci 2023, 24, 6642. [PubMed: 37047615]

(83). Verkhivker G; Alshahrani M; Gupta G Balancing Functional Tradeoffs between Protein Stability and ACE2 Binding in the SARS-CoV-2 Omicron BA.2, BA.2.75 and XBB Lineages: Dynamics-Based Network Models Reveal Epistatic Effects Modulating Compensatory Dynamic and Energetic Changes. Viruses 2023, 15, 1143. [PubMed: 37243229]

(84). Tian H; Jiang X; Tao P PASSer: Prediction of Allosteric Sites Server. Mach Learn Sci Technol. 2021, 2, No. 035015.

(85). Xiao S; Tian H; Tao P PASSer2.0: Accurate Prediction of Protein Allosteric Sites Through Automated Machine Learning. Front. Mol. Biosci 2022, 9, No. 879251.

(86). Tian H; Xiao S; Jiang X; Tao P PASSerRank: Prediction of Allosteric Sites with Learning to Rank. ArXiv, 2023.

(87). Tian H; Xiao S; Jiang X; Tao P PASSer: Fast and Accurate Prediction of Protein Allosteric Sites. Nucleic Acids Res. 2023, 51, W427–W431. [PubMed: 37102691]

(88). Rose PW; Prlic A; Altunkaya A; Bi C; Bradley AR; Christie CH; Costanzo LD; Duarte JM; Dutta S; Feng Z; Green RK; Goodsell DS; Hudson B; Kalro T; Lowe R; Peisach E; Randle C; Rose AS; Shao C; Tao YP; Valasatava Y; Voigt M; Westbrook JD; Woo J; Yang H; Young JY; Zardecki C; Berman HM; Burley SK The RCSB protein data bank: integrative view of protein, gene and 3D structural information. Nucleic Acids Res. 2017, 45, D271–D281. [PubMed: 27794042]

(89). Hekkelman ML; Te Beek TA; Pettifer SR; Thorne D; Attwood TK; Vriend G WIWS: A protein structure bioinformatics web service collection. Nucleic Acids Res. 2010, 38, W719–W723. [PubMed: 20501602]

(90). Fernandez-Fuentes N; Zhai J; Fiser A ArchPRED: A template based loop structure prediction server. Nucleic Acids Res. 2006, 34, W173–W176. [PubMed: 16844985]

(91). Krivov GG; Shapovalov MV; Dunbrack RL Jr. Improved prediction of protein side-chain conformations with SCWRL4. Proteins 2009, 77, 778–795. [PubMed: 19603484]

(92). Bhattacharya D; Nowotny J; Cao R; Cheng J 3Drefine: An Interactive Web Server for Efficient Protein Structure Refinement. Nucleic Acids Res. 2016, 44, W406–W409. [PubMed: 27131371]

(93). Olsson MHM; Søndergaard CR; Rostkowski M; Jensen JH PROPKA3: consistent treatment of internal and surface residues in empirical pKa predictions. J. Chem. Theory Comput 2011, 7, 525–537. [PubMed: 26596171]

(94). Li M; Simonetti FL; Goncearenco A; Panchenko AR MutaBind estimates and interprets the effects of sequence variants on protein-protein interactions. Nucleic Acids Res. 2016, 44, W494–W501. [PubMed: 27150810]

(95). Zhang N; Chen Y; Lu H; Zhao F; Alvarez RV; Goncearenco A; Panchenko AR; Li M. MutaBind2: Predicting the Impacts of Single and Multiple Mutations on Protein-Protein Interactions. iScience 2020, 23, No. 100939.

(96). Schymkowitz J; Borg J; Stricher F; Nys R; Rousseau F; Serrano L The FoldX Web Server: An Online Force Field. Nucleic Acids Res. 2005, 33, W382–W388. [PubMed: 15980494]

(97). Van Durme J; Delgado J; Stricher F; Serrano L; Schymkowitz J; Rousseau F A Graphical Interface for the FoldX Force Field. Bioinformatics 2011, 27, 1711–1712. [PubMed: 21505037]

(98). Phillips JC; Braun R; Wang W; Gumbart J; Tajkhorshid E; Villa E; Chipot C; Skeel RD; Kalé L; Schulten K Scalable molecular dynamics with NAMD. J. Comput. Chem 2005, 26, 1781–1802. [PubMed: 16222654]

(99). Huang J; Rauscher S; Nawrocki G; Ran T; Feig M; de Groot BL; Grubmüller H; MacKerell AD Jr. CHARMM36m: an improved force field for folded and intrinsically disordered proteins. Nat. Methods 2017, 14, 71–73. [PubMed: 27819658]

(100). Jorgensen WL; Chandrasekhar J; Madura JD; Impey RW; Klein ML Comparison of Simple Potential Functions for Simulating Liquid Water. J. Chem. Phys 1983, 79, 926–935.

(101). Fernandes HS; Sousa SF; Cerqueira NMFSA VMD Store-A VMD Plugin to Browse, Discover, and Install VMD Extensions. J. Chem. Inf. Model 2019, 59, 4519–4523. [PubMed: 31682440]

(102). Ryckaert J-P; Ciccotti G; Berendsen HJC Numerical Integration of the Cartesian Equations of Motion of a System with Constraints: Molecular Dynamics of n-Alkanes.J. Comput. Phys 1977, 23, 327–341.

(103). Di Pierro M; Elber R; Leimkuhler B A Stochastic Algorithm for the Isobaric-Isothermal Ensemble with Ewald Summations for All Long Range Forces. J. Chem. Theory Comput 2015, 11, 5624–5637. [PubMed: 26616351]

(104). Eastman P; Swails J; Chodera JD; McGibbon RT; Zhao Y; Beauchamp KA; Wang L-P; Simmonett AC; Harrigan MP; Stern CD; Wiewiora RP; Brooks BR; Pande VS OpenMM 7: Rapid Development of High Performance Algorithms for Molecular Dynamics. PLoS Comput. Biol 2017, 13, No. e1005659.

(105). Naritomi Y; Fuchigami S Slow Dynamics in Protein Fluctuations Revealed by Time-Structure Based Independent Component Analysis: The Case of Domain Motions. J. Chem. Phys 2011, 134, No. 065101.

(106). Schwantes CR; Pande VS Improvements in Markov State Model Construction Reveal Many Non-Native Interactions in the Folding of NTL9. J. Chem. Theory Comput 2013, 9, 2000–2009. [PubMed: 23750122]

(107). M Sultan M; Pande VS tICA-Metadynamics: Accelerating Metadynamics by Using Kinetically Selected Collective Variables. J. Chem. Theory Comput 2017, 13, 2440–2447. [PubMed: 28383914]

(108). Trozzi F; Wang X; Tao P UMAP as a Dimensionality Reduction Tool for Molecular Dynamics Simulations of Biomacromolecules: A Comparison Study. J. Phys. Chem. B 2021, 125, 5022–5034. [PubMed: 33973773]

(109). Scherer MK; Trendelkamp-Schroer B; Paul F; Pérez-Hernández G; Hoffmann M; Plattner N; Wehmeyer C; Prinz J-H; Noé F PyEMMA 2: A Software Package for Estimation, Validation, and Analysis of Markov Models. J. Chem. Theory Comput 2015, 11, 5525–5542. [PubMed: 26574340]

(110). Wu H; Paul F; Wehmeyer C; Noe F Multiensemble Markov models of molecular thermodynamics and kinetics. Proc. Natl. Acad. Sci. U.S.A 2016, 113, E3221–E3230. [PubMed: 27226302]

(111). Suárez E; Adelman JL; Zuckerman DM Accurate Estimation of Protein Folding and Unfolding Times: Beyond Markov State Models. J. Chem. Theory Comput 2016, 12, 3473–3481. [PubMed: 27340835]

(112). Bowman GR; Bolin ER; Hart KM; Maguire BC; Marqusee S Discovery of multiple hidden allosteric sites by combining Markov state models and experiments. Proc. Natl. Acad. Sci. U.S.A 2015, 112, 2734–2739. [PubMed: 25730859]

(113). Bowman GR; Noé F Software for Building Markov State Models. Adv. Exp. Med. Biol 2014, 797, 139. [PubMed: 24297281]

(114). Bowman GR A Tutorial on Building Markov State Models with MSMBuilder and Coarse-Graining Them with BACE. Methods Mol. Biol 2014, 1084, 141–158. [PubMed: 24061920]

(115). Trendelkamp-Schroer B; Wu H; Paul F; Noé F Estimation and Uncertainty of Reversible Markov Models. J. Chem. Phys 2015, 143, No. 174101.

(116). Bowman GR; Huang X; Pande VS Using Generalized Ensemble Simulations and Markov State Models to Identify Conformational States. Methods 2009, 49, 197–201. [PubMed: 19410002]

(117). Atilgan C; Atilgan AR Perturbation-response scanning reveals ligand entry-exit mechanisms of ferric binding protein. PLoS Comput. Biol 2009, 5, No. e1000544.

(118). Atilgan C; Gerek ZN; Ozkan SB; Atilgan AR Manipulation of conformational change in proteins by single-residue perturbations. Biophys. J 2010, 99, 933–943. [PubMed: 20682272]

(119). Jalalypour F; Sensoy O; Atilgan C Perturb-Scan-Pull: A Novel Method Facilitating Conformational Transitions in Proteins. J. Chem. Theory Comput 2020, 16, 3825–3841. [PubMed: 32324386]

(120). Penkler D; Sensoy Ö; Atilgan C; Tastan Bishop Ö Perturbation-Response Scanning Reveals Key Residues for Allosteric Control in Hsp70. J. Chem. Inf. Model 2017, 57, 1359–1374 Jun 26. [PubMed: 28505454]

(121). General IJ; Liu Y; Blackburn ME; Mao W; Gierasch LM; Bahar I ATPase subdomain IA is a mediator of interdomain allostery in Hsp70 molecular chaperones. PLoS Comput. Biol 2014, 10, No. e1003624.

(122). Dutta A; Krieger J; Lee JY; Garcia-Nafria J; Greger IH; Bahar I Cooperative Dynamics of Intact AMPA and NMDA Glutamate Receptors: Similarities and Subfamily-Specific Differences. Structure 2015, 23, 1692–1704. [PubMed: 26256538]

(123). Stetz G; Tse A; Verkhivker GM Dissecting Structure-Encoded Determinants of Allosteric Cross-Talk between Post-Translational Modification Sites in the Hsp90 Chaperones. Sci. Rep 2018, 8, No. 6899.

(124). Verkhivker GM; Di Paola L Dynamic Network Modeling of Allosteric Interactions and Communication Pathways in the SARS-CoV-2 Spike Trimer Mutants: Differential Modulation of Conformational Landscapes and Signal Transmission via Cascades of Regulatory Switches. J. Phys. Chem. B 2021, 125, 850–873. [PubMed: 33448856]

(125). Xiao S; Verkhivker GM; Tao P Machine Learning and Protein Allostery. Trends Biochem. Sci 2023, 48, 375–390. [PubMed: 36564251]

(126). Huang Z; Zhu L; Cao Y; Wu G; Liu X; Chen Y; Wang Q; Shi T; Zhao Y; Wang Y; Li W; Li Y; Chen H; Chen G; Zhang J ASD: A Comprehensive Database of Allosteric Proteins and Modulators. Nucleic Acids Res. 2011, 39, D663–D669. [PubMed: 21051350]

(127). Lu S; Shen Q; Zhang J Allosteric Methods and Their Applications: Facilitating the Discovery of Allosteric Drugs and the Investigation of Allosteric Mechanisms. Acc. Chem. Res. 2019, 52, 492–500. [PubMed: 30688063]

(128). Zlobin AS; Suplatov D; Kopylov K; švedas V CASBench: A Benchmarking Set of Proteins with Annotated Catalytic and Allosteric Sites in Their Structures. Acta Naturae 2019, 11, 74–80. [PubMed: 31024751]

(129). Schmidtke P; Le Guilloux V; Maupetit J; Tuffery P Fpocket: Online Tools for Protein Ensemble Pocket Detection and Tracking. Nucleic Acids Res. 2010, 38, W582–W589. [PubMed: 20478829]

(130). Ke G; Meng Q; Finley T; Wang T; Chen W; Ma W; Ye Q; Liu T-Y In Lightgbm: A Highly Efficient Gradient Boosting Decision Tree. Advances in Neural Information Processing Systems, 30. Proceedings of 31st Conference on Neural Information Processing Systems (NIPS 2017), Long Beach, CA, USA, 2017.

(131). Scarpa F; Sanna D; Benvenuto D; Borsetti A; Azzena I; Casu M; Fiori PL; Giovanetti M; Maruotti A; Ceccarelli G; Caruso A; Caccuri F; Cauda R; Cassone A; Pascarella S; Ciccozzi M Genetic and Structural Data on the SARS-CoV-2 Omicron BQ.1 Variant Reveal Its Low Potential for Epidemiological Expansion. Int. J. Mol Sci 2022, 23, 15264. [PubMed: 36499592]

(132). Qu P; Evans JP; Faraone JN; Zheng Y-M; Carlin C; Anghelina M; Stevens P; Fernandez S; Jones D; Lozanski G; Panchal A; Saif LJ; Oltz EM; Xu K; Gumina RJ; Liu S-L Enhanced Neutralization Resistance of SARS-CoV-2 Omicron Subvariants BQ.1, BQ.1.1, BA.4.6, BF.7, and BA.2.75.2. Cell Host Microbe 2023, 31, 9–17.e3. [PubMed: 36476380]

(133). Sacquin-Mora S; Lavery R Investigating the local flexibility of functional residues in hemoproteins. Biophys. J 2006, 90, 2706–2717. [PubMed: 16428284]

(134). Sacquin-Mora S; Laforet E; Lavery R Locating the active sites of enzymes using mechanical properties. Proteins 2007, 67, 350–359. [PubMed: 17311346]

(135). Starr TN; Greaney AJ; Hilton SK; Ellis D; Crawford KHD; Dingens AS; Navarro MJ; Bowen JE; Tortorici MA; Walls AC; King NP; Veesler D; Bloom JD Deep Mutational Scanning of SARS-CoV-2 Receptor Binding Domain Reveals Constraints on Folding and ACE2 Binding. Cell 2020, 182, 1295–1310.e20. [PubMed: 32841599]

(136). Starr TN; Greaney AJ; Stewart CM; Walls AC; Hannon WW; Veesler D; Bloom JD Deep Mutational Scans for ACE2 Binding, RBD Expression, and Antibody Escape in the SARS-CoV-2 Omicron BA.1 and BA.2 Receptor-Binding Domains. PLoS Pathog. 2022, 18, No. e1010951.

(137). Greaney AJ; Starr TN; Bloom JD An Antibody-Escape Estimator for Mutations to the SARS-CoV-2 Receptor-Binding Domain. Virus Evol. 2022, 8, No. veac021.

(138). Raman AS; White KI; Ranganathan R Origins of Allostery and Evolvability in Proteins: A Case Study. Cell 2016, 166, 468–480. [PubMed: 27321669]

(139). Kim I; Dubrow A; Zuniga B; Zhao B; Sherer N; Bastiray A; Li P; Cho J-H Energy Landscape Reshaped by Strain-Specific Mutations Underlies Epistasis in NS1 Evolution of Influenza A Virus. Nat. Commun 2022, 13, No. 5775.

(140). Tee W-V; Guarnera E; Berezovsky IN Reversing allosteric communication: From detecting allosteric sites to inducing and tuning targeted allosteric response. PLoS Comput. Biol 2018, 14, No. e1006228.

(141). Fan J; Liu Y; Kong R; Ni D; Yu Z; Lu S; Zhang J Harnessing Reversed Allosteric Communication: A Novel Strategy for Allosteric Drug Discovery. J. Med. Chem 2021, 64, 17728–17743. [PubMed: 34878270]

(142). Ni D; Wei J; He X; Rehman AU; Li X; Qiu Y; Pu J; Lu S; Zhang J Discovery of cryptic allosteric sites using reversed allosteric communication by a combined computational and experimental strategy. Chem. Sci 2021, 12, 464–476.

(143). Toelzer C; Gupta K; Yadav SKN; Borucu U; Davidson AD; Kavanagh Williamson M; Shoemark DK; Garzoni F; Staufer O; Milligan R; Capin J; Mulholland AJ; Spatz J; Fitzgerald D; Berger I; Schaffitzel C Free fatty acid binding pocket in the locked structure of SARS-CoV-2 spike protein. Science 2020, 370, 725–730. [PubMed: 32958580]

(144). Krivák R; Hoksza D P2Rank: Machine Learning Based Tool for Rapid and Accurate Prediction of Ligand Binding Sites from Protein Structure. J. Cheminform 2018, 10, 39. [PubMed: 30109435]

(145). Jakubec D; Skoda P; Krivak R; Novotny M; Hoksza D PrankWeb 3: Accelerated Ligand-Binding Site Predictions for Experimental and Modelled Protein Structures. Nucleic Acids Res. 2022, 50, W593–W597. [PubMed: 35609995]
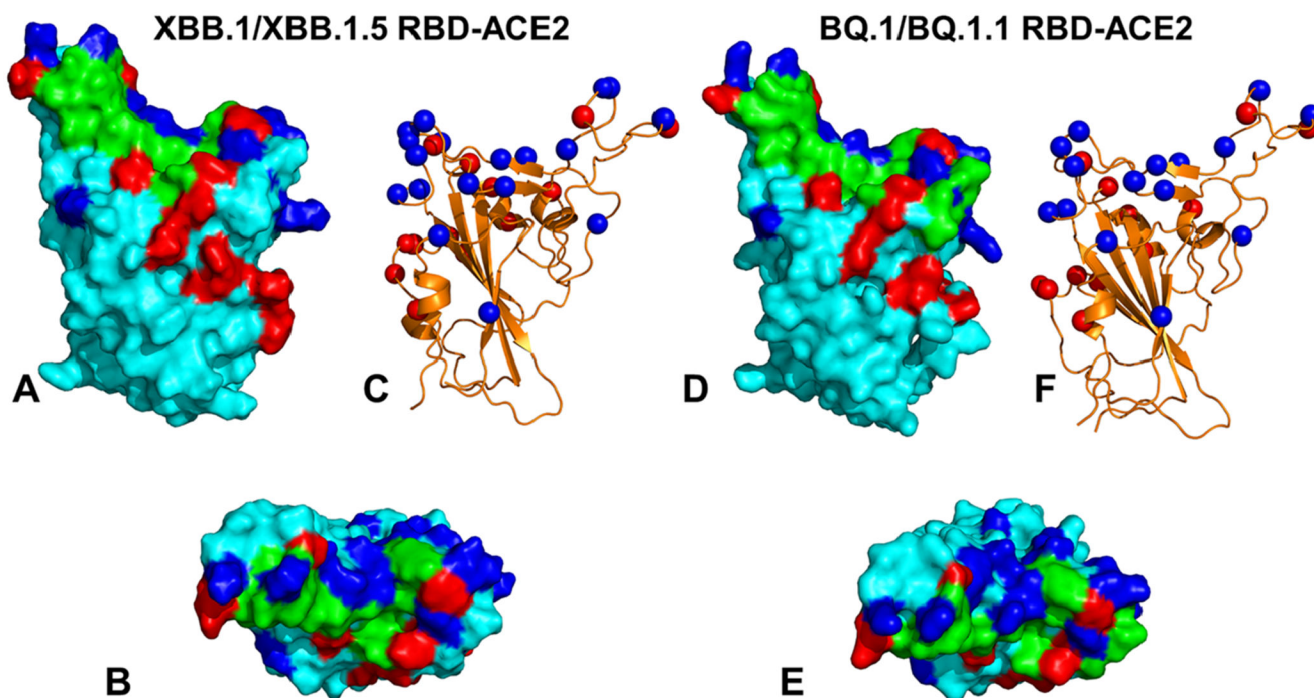
Figure 1.
Structural organization and binding epitopes of the SARS-CoV-2 RBD Omicron XBB.1/ XBB.1.5 and BQ.1/BQ.1.1 complexes with human ACE enzyme. (A) The optimized modeled structure of the Omicron RBD XBB.1/XBB.1.5-ACE2 complex (only RBD is shown). The RBD is in the cyan surface, the binding epitope is in the green surface, XBB.1/XBB.1.5 Omicron mutations are in red, and the convergent mutational sites are in the blue surface. (B) Top view of the RBD XBB.1/XBB.1.5 from complexes with ACE2. (C) Omicron RBD XBB.1/XBB.1.5 in ribbon representation. The sites of convergent mutations are in blue spheres. (D) Optimized modeled structure of the Omicron RBD BQ.1/BQ.1.1-ACE2 complex (only RBD is shown). The RBD is in the cyan surface, the binding epitope is in the green surface, BQ.1/BQ.1.1 Omicron mutations are in red, and the convergent mutational sites (R346T, K356, N440K, K444T, V445, G446, N450, L452R, N460K, T478K, E484A, F486V, F490, Q493, S494, and N501Y) are in the blue surface. (E) Top view of the RBD BQ.1/BQ.1.1 from complexes with ACE2. (F) Omicron RBD BQ.1/BQ.1.1 in ribbon representation. The sites of convergent mutations are shown in blue spheres.
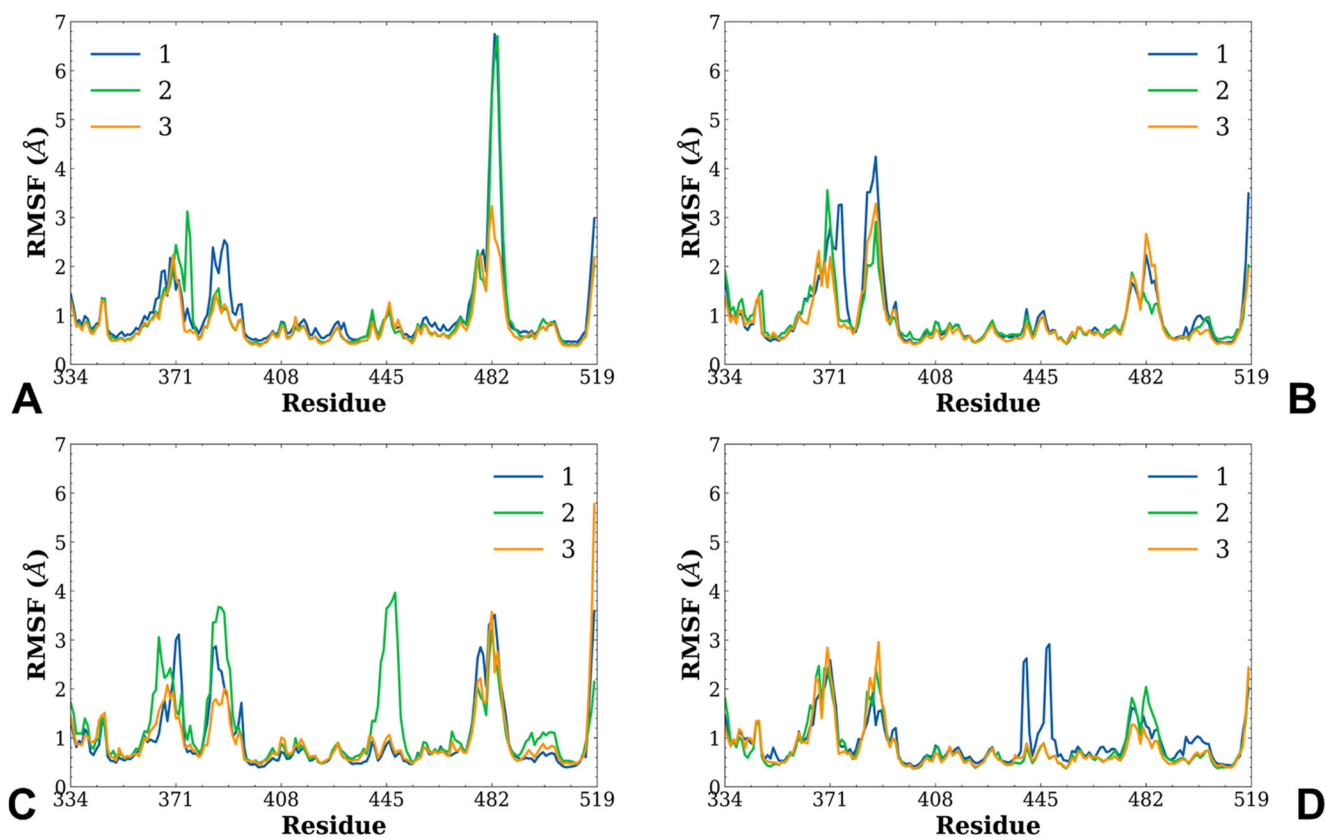
Figure 2.
Conformational dynamics profiles obtained from three independent MD simulations of the Omicron RBD XBB.1, XBB.1.5, BQ.1, and BQ.1.1 complexes with ACE2. The RMSF profiles for the RBD residues obtained from three independent microsecond MD simulations of the Omicron XBB.1 RBD-ACE2 (A), Omicron XBB.1.5 RBD-ACE2 (B), Omicron BQ.1 RBD-ACE2 (C), and Omicron BQ.1.1 RBD-ACE2 complexes (D).
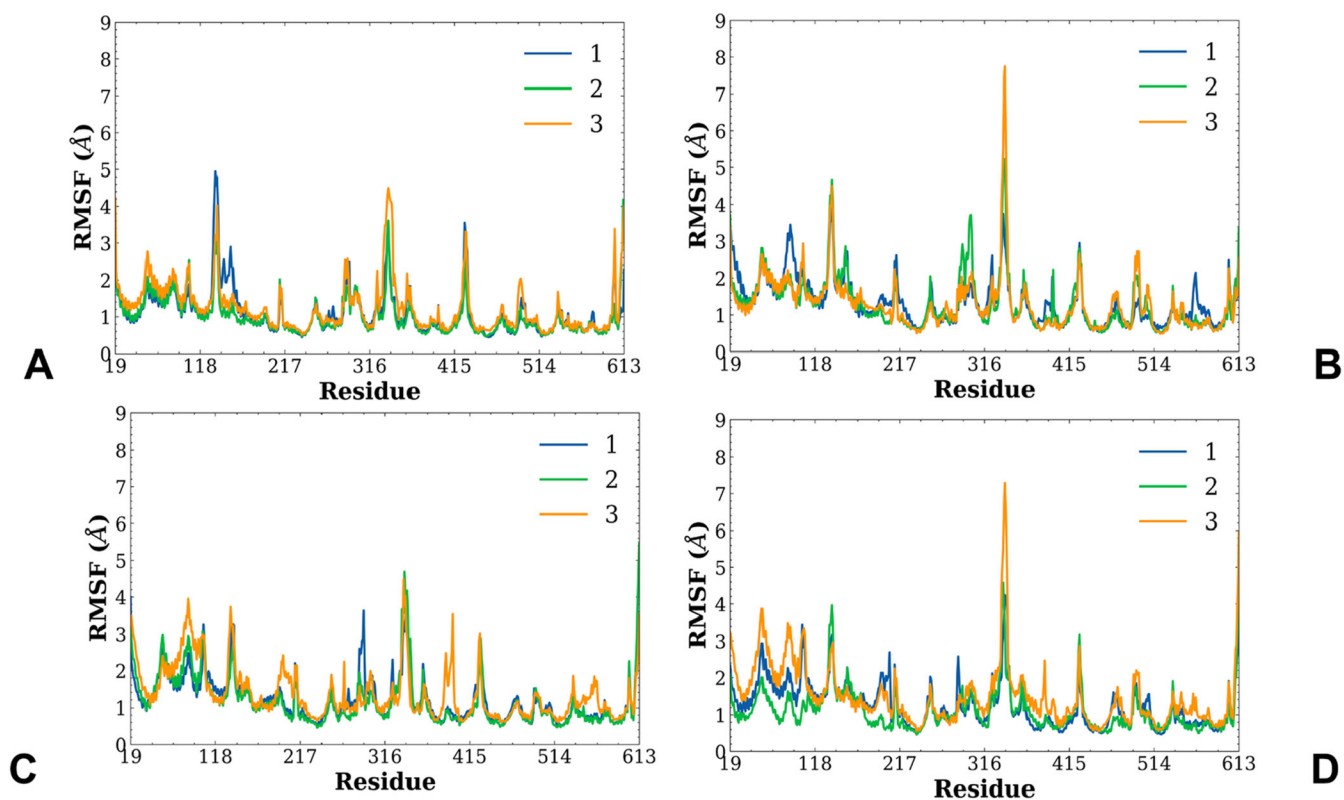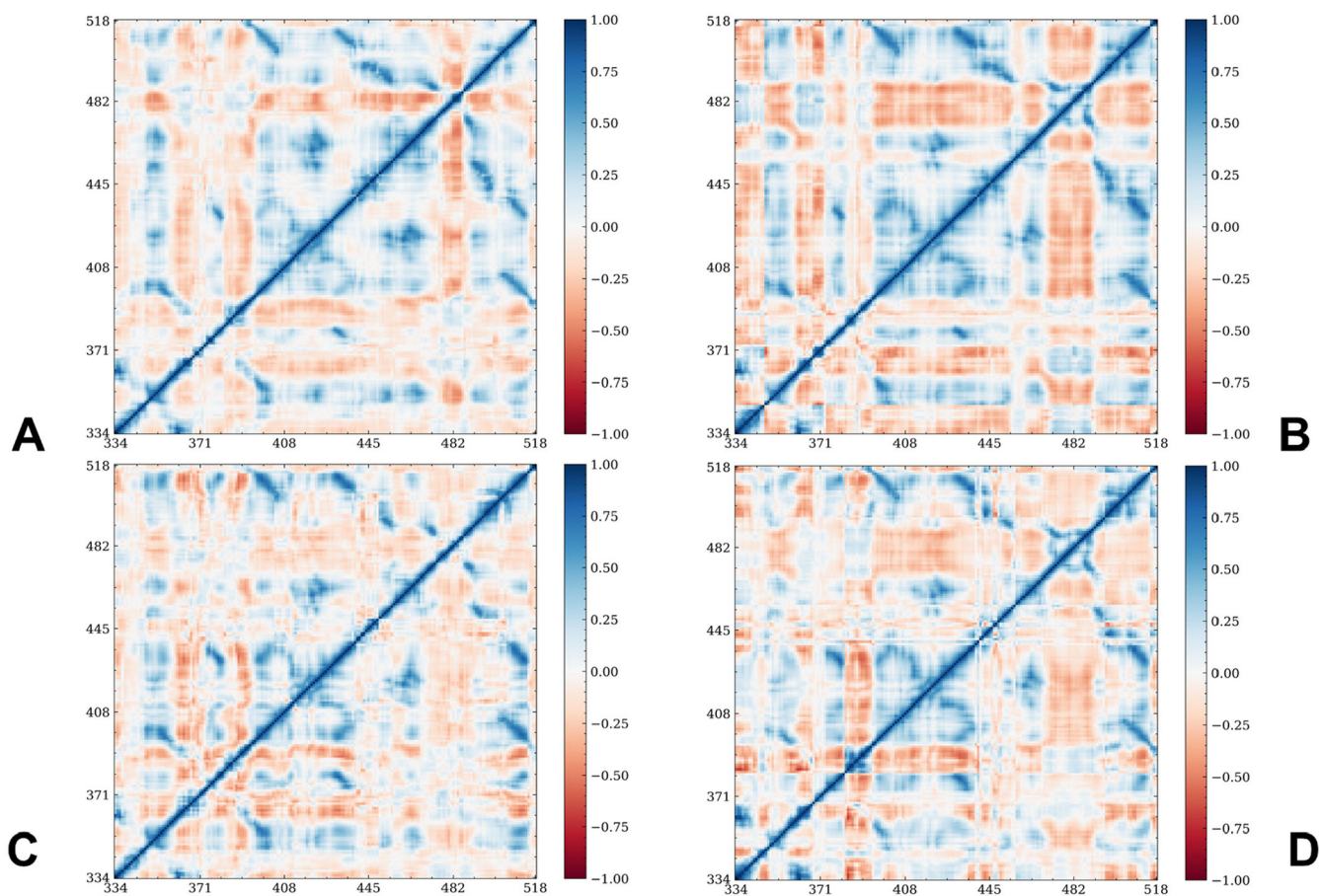
Figure 3.
Conformational dynamics profiles of the ACE2 residues obtained from three independent
MD simulations of the Omicron RBD XBB.1, XBB.1.5, BQ.1, and BQ.1.1 complexes
with ACE2. The RMSF profiles for the ACE2 backbone residues obtained from three
independent microsecond MD simulations of the Omicron XBB.1 RBD-ACE2 (A), Omicron
XBB.1.5 RBD-ACE2 (B), Omicron BQ.1 RBD-ACE2 (C), and Omicron BQ.1.1 RBD-
ACE2 complexes (D).

Figure 4.
DCC for the RBD residues in the Omicron XBB.1 RBD-ACE2 (A), Omicron XBB.1.5 RBD-ACE2 (B), Omicron BQ.1 RBD-ACE2 (C), and Omicron BQ.1.1 RBD-ACE2 (D) complexes.
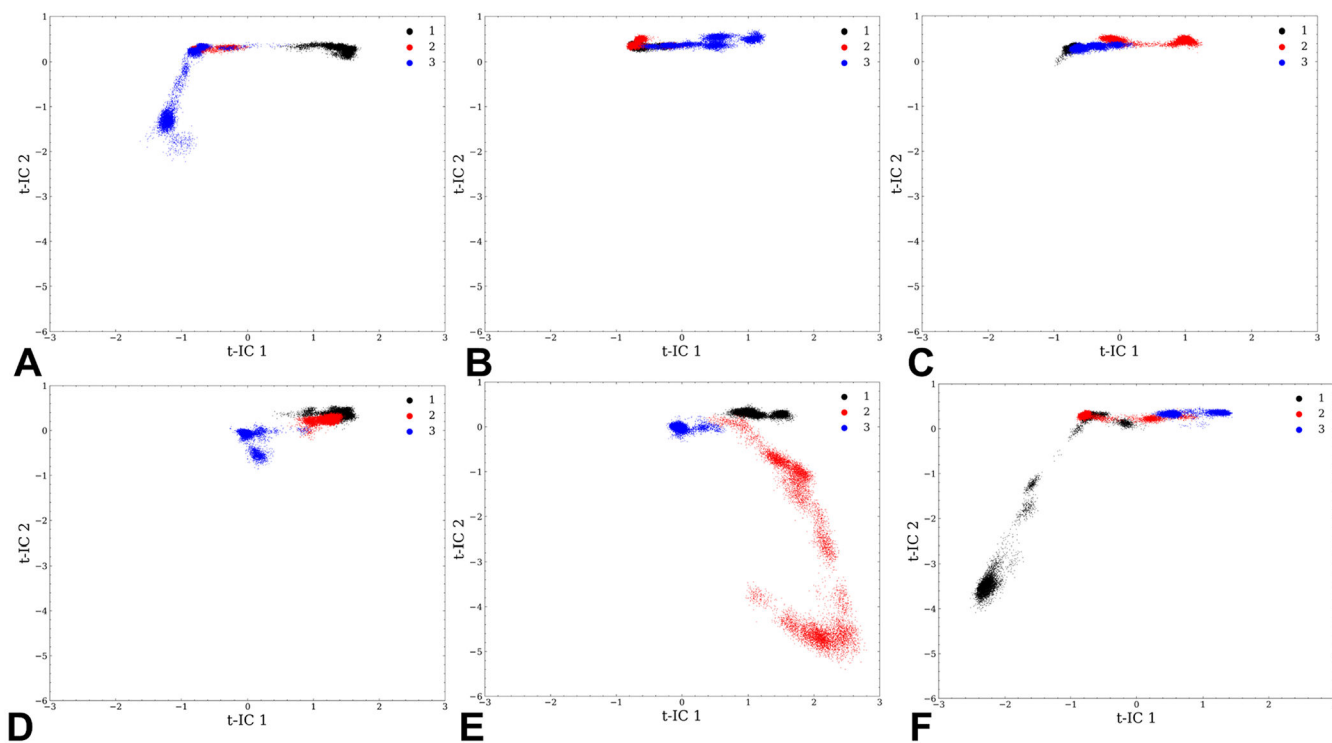
Figure 5.
tICA low-dimensional projection of the conformational space sampled in three independent microsecond MD simulations for the Omicron BA.2 RBD-ACE2 (A), XBB.1 RBD-ACE2 (B), and Omicron XBB.1.5 RBD-ACE2 (C). tICA low-dimensional projection of the conformational space for Omicron BA.4/BA.5 RBD-ACE2 (D), BQ.1 RBD-ACE2 (E), and Omicron BQ.1.1 RBD-ACE2 (F) complexes. The densities are shown in black dots for MD trajectory 1, in red dots for MD trajectory 2, and in blue dots for MD trajectory 3.
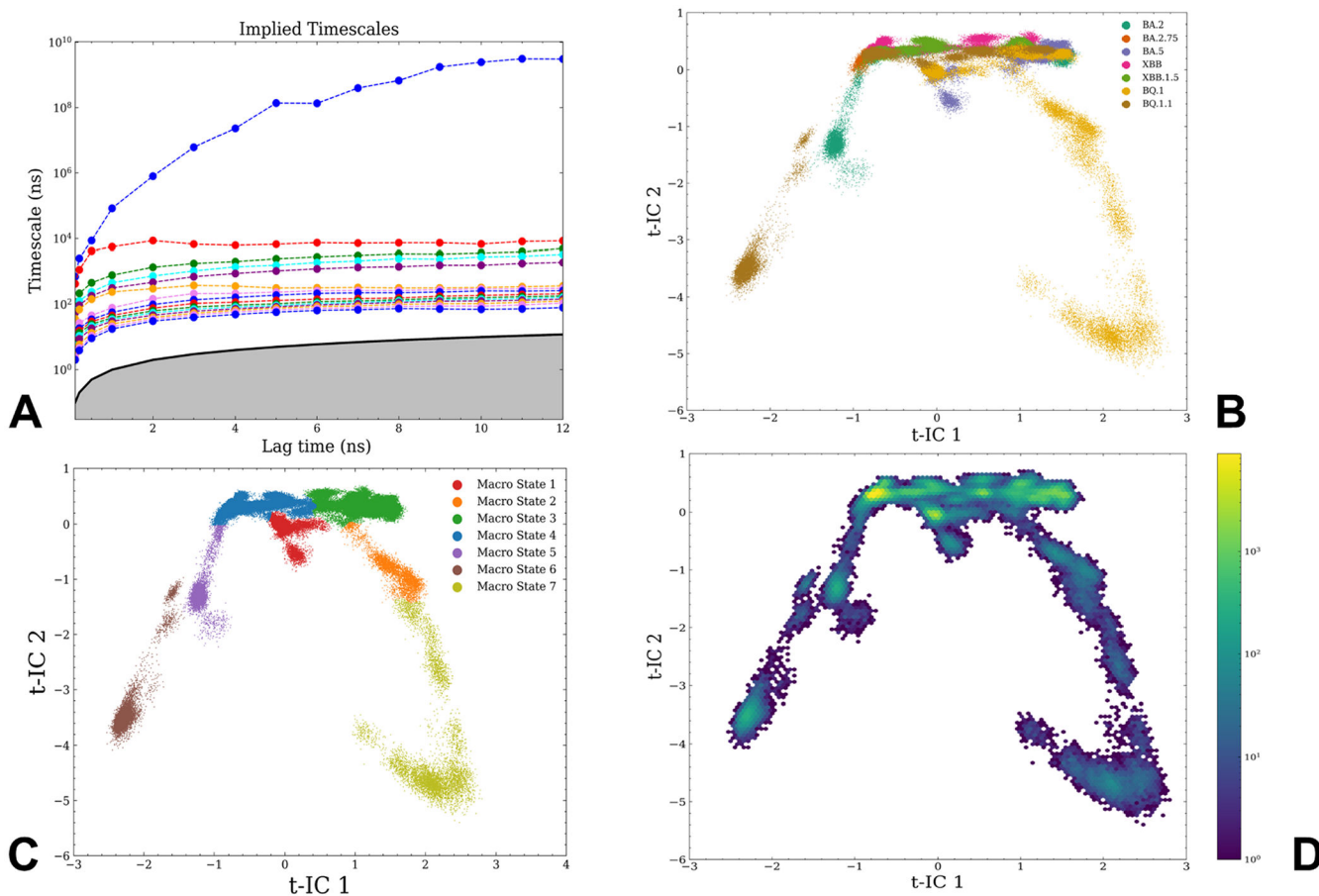
Figure 6.
MSM analysis of the conformational landscapes for Omicron RBD-ACE2 complexes. (A) The estimated relaxation timescale is based on the transition probabilities among different microstates using different lag times ranging from 0.1 to 12 ns. The top 15 timescales are shown. Each line represents the implied timescale as a function of the lag time, and it is based on the corresponding eigenvalue. The estimated timescale converged after ~5 ns, which was chosen as the lag time in the construction of MSM. The gray area depicts a "linear" region where the lag time (*x* axis) equals the relaxation timescale (*y* axis) but note that y axis is shown in the log scale. The implied timescales crossing under the gray region correspond to processes which are faster than the lag time and, thus, are not resolved. (B) The low-dimensional density representation with 2 components (t-IC) is constructed for all simulated systems. The distribution densities are colored based on the system and are shown for BA.2 (in emerald green), BA.2.75 (burnt Sienna), BA.5 (purple), XBB.1 (pink), XBB.1.5 (forest green), BQ.1 (earthy yellow), and BQ.1.1 variants (brown). (C) The low-dimensional density representations with 2 components (t-IC) are shown for macrostate 1 (red), macrostate 2 (orange), macrostate 3 (green), macrostate 4 (blue), macrostate 5 (purple), macrostate 6 (brown), and macrostate 7 (lime zest). (D) The distribution density of all simulations is visualized using a hexagon bin plot. Each hexagon represents a small region, and the color bar shows the frequency of this region.
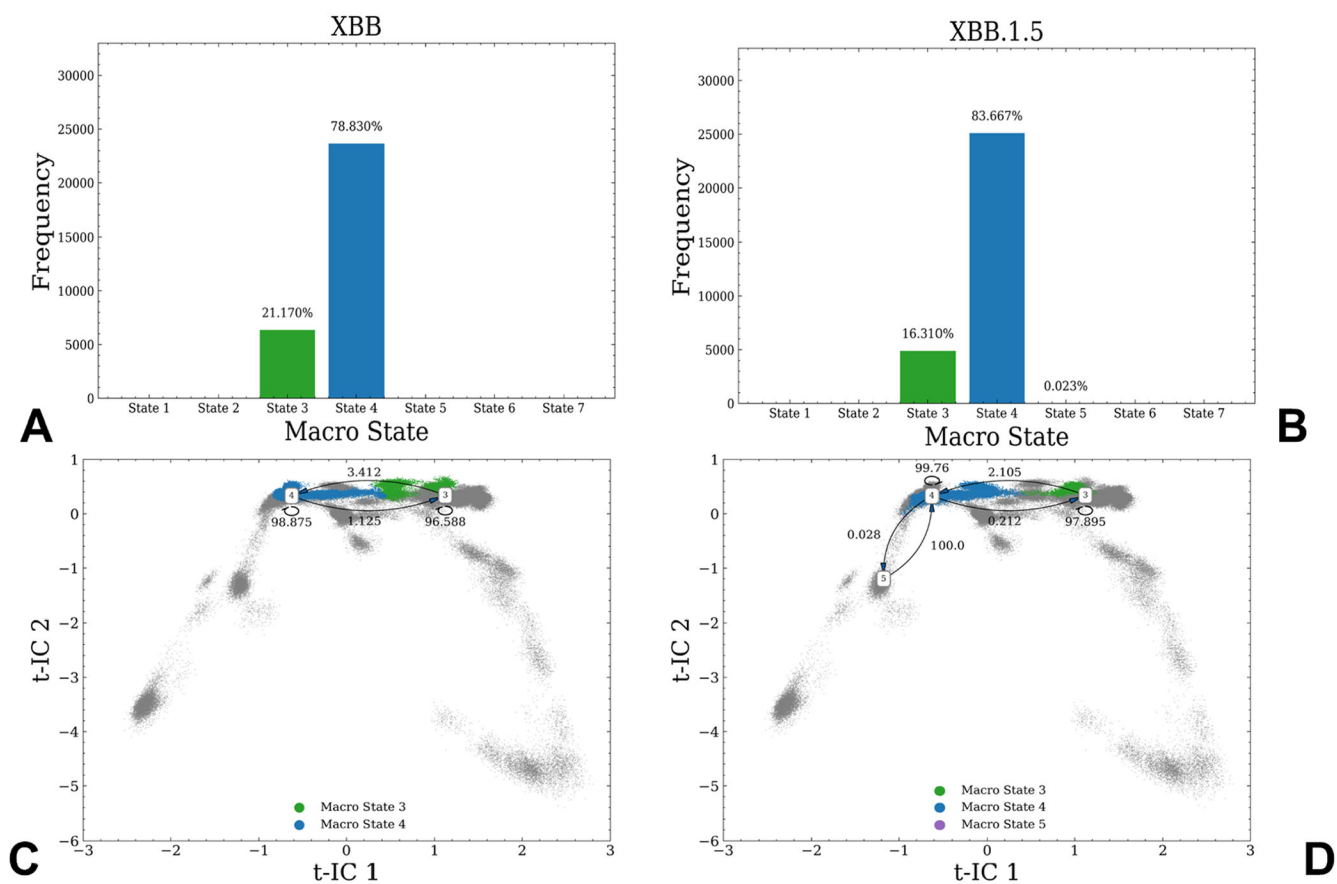
Figure 7.
MSM analysis of the conformational landscape for XBB.1 and XBB.1.5 RBD-ACE2 complexes. The frequency distribution of occupying different macrostates in XBB.1 (A) and XBB.1.5 (B). Transition probability maps among different macrostates with the 5 ns lag time for XBB.1 (C) and XBB.1.5 variant (D). The high percentage of self-conserved probability shows the stability of macrostates.
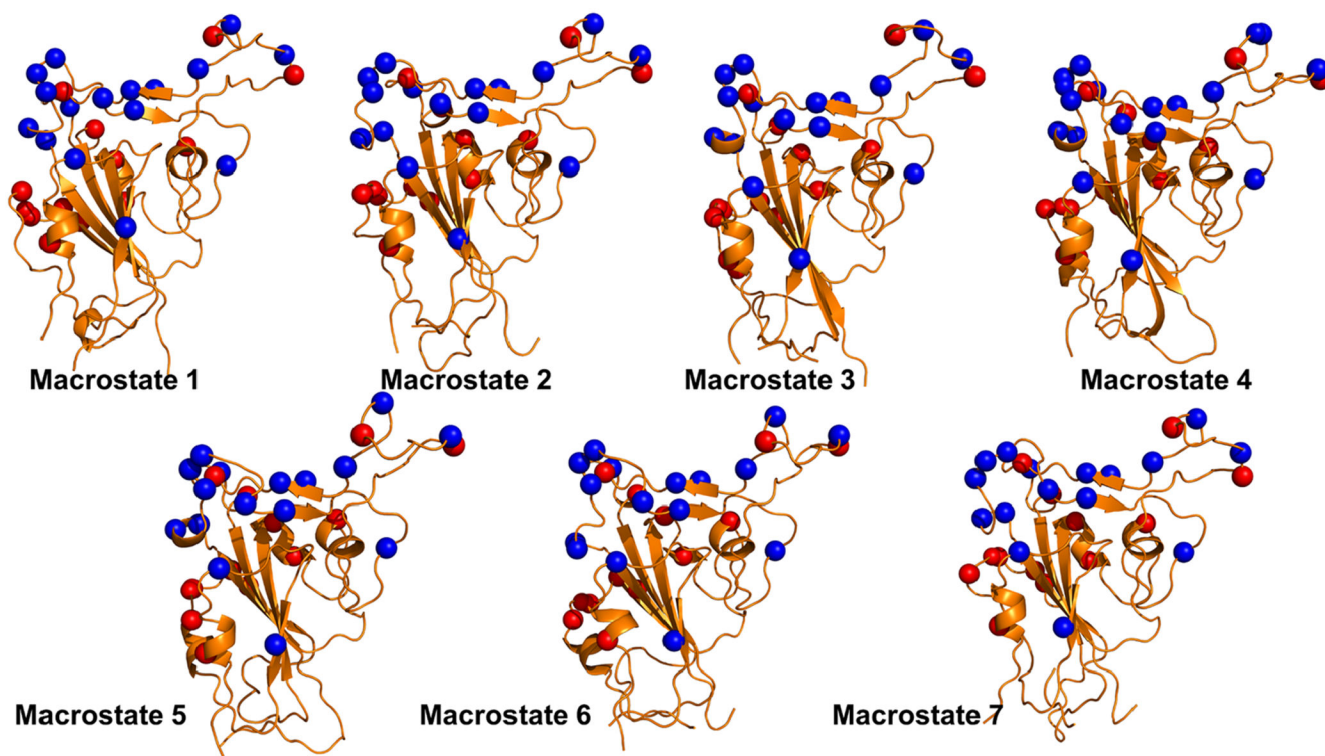
Figure 8.
Structural analysis of macrostates determined in the MSM analysis. To perform a comparative structural analysis of obtained macrostates, the assignments of all points are examined to determine which point belongs to which macrostate. By calculating the centroid of the conformations that belong to each macrostate, the closest to the centroid existing frame is determined and considered as a representative of a given macrostate. The macrostates are annotated and are shown in orange-colored ribbons. The convergent mutation sites are highlighted in blue spheres. The analysis shows differences between conformations that are particularly exemplified by changes in the flexible loops 440–452 and 470–491.
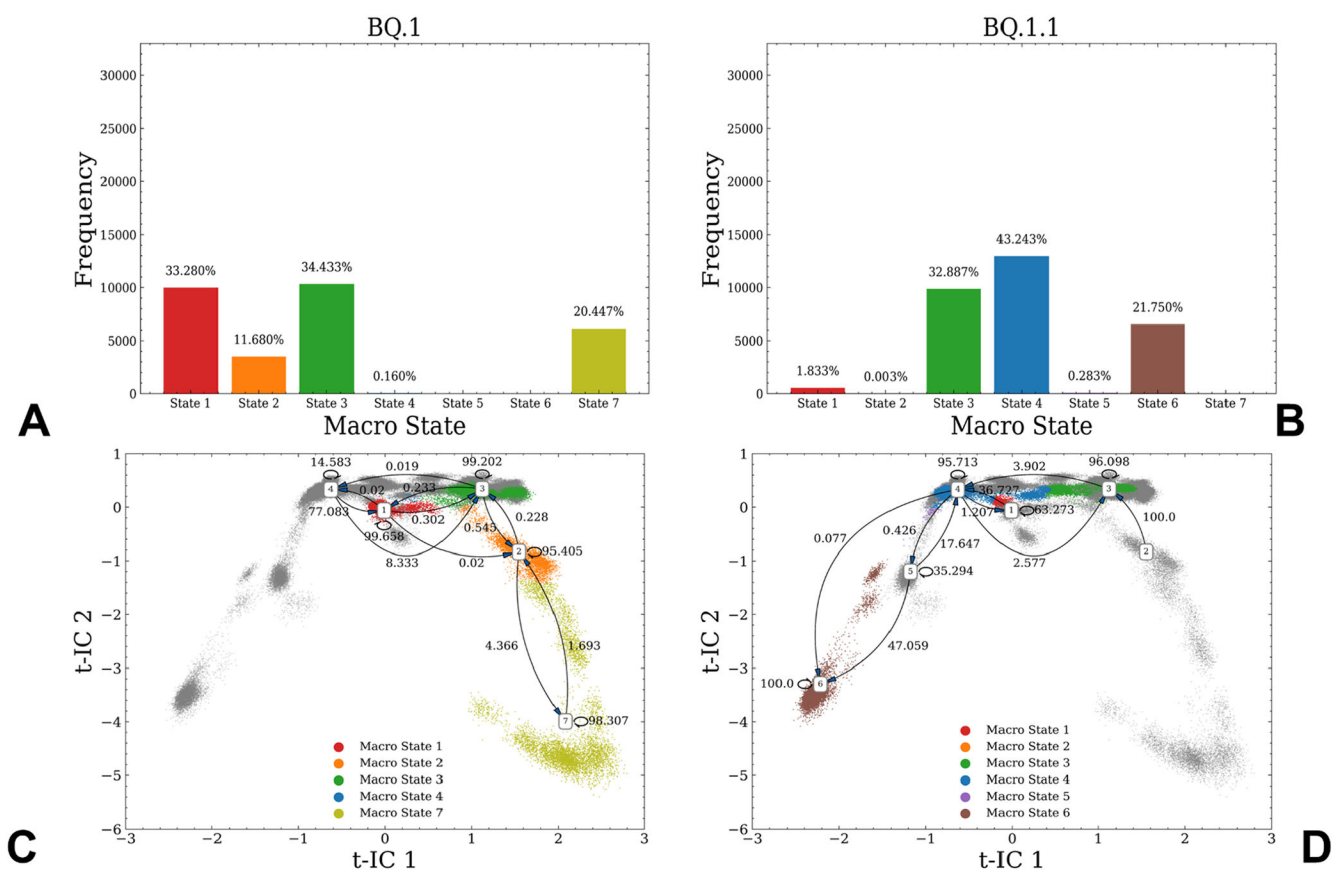
Figure 9.

MSM analysis of the conformational landscape for BQ.1 and BQ.1.1 RBD-ACE2 complexes. The frequency distribution of occupying different macrostates in BQ.1 (A) and BQ.1.1 (B). Transition probability maps among different macrostates with the 5 ns lag time for BQ.1 (C) and BQ.1.1 variant (D). The high percentage of self-conserved probability shows the stability of macrostates.
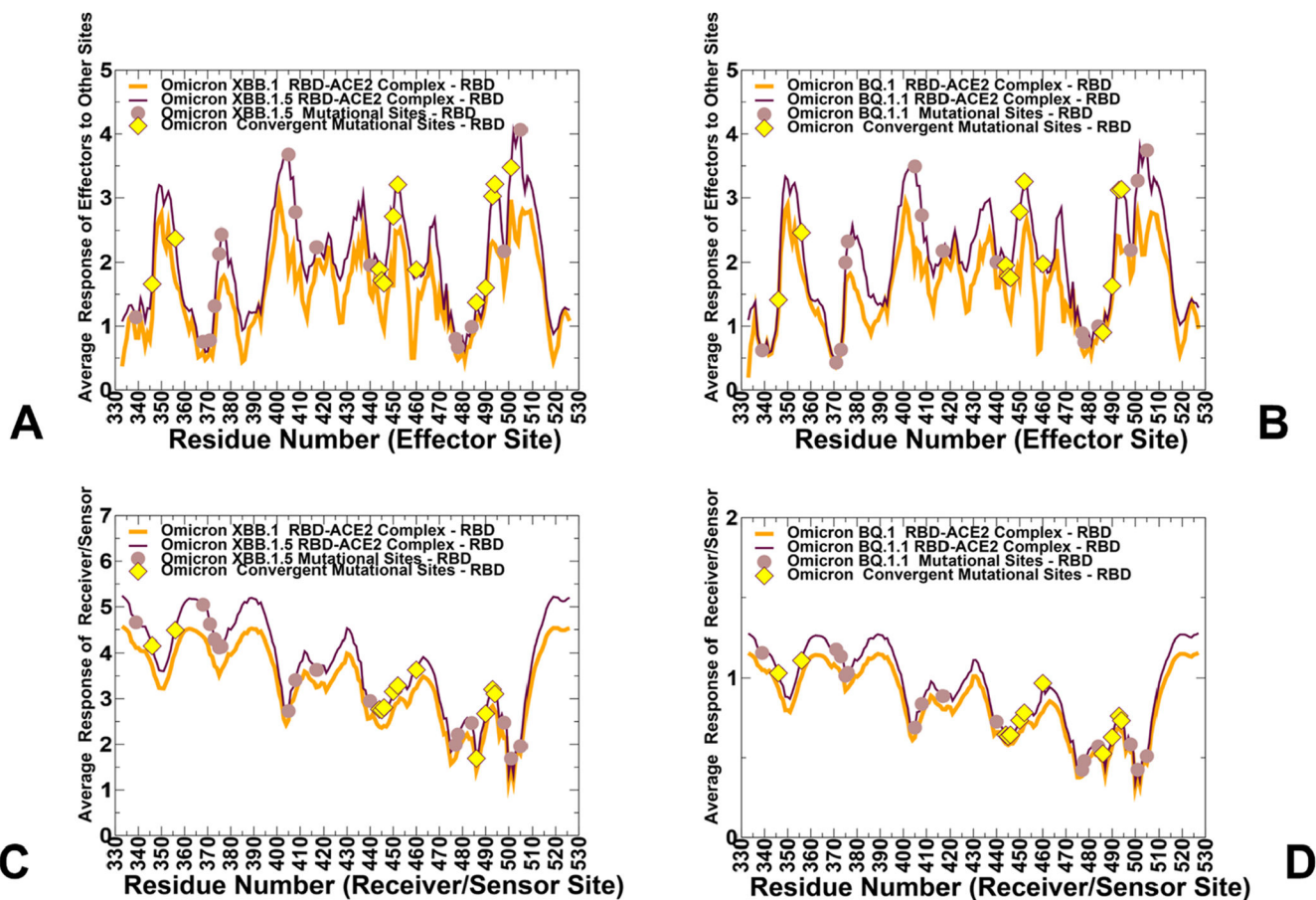
Figure 10.
PRS analysis of the SARS-CoV-2 Omicron RBD-ACE2 complexes. (A) PRS effector profiles for the XBB.1 RBD (in orange lines) and XBB.1.5 RBD (in maroon lines). (B) PRS effector profiles for the BQ.1 RBD (in orange lines) and BQ.1.1 RBD (in maroon lines). (C) PRS sensor profiles for the XBB.1 RBD (in orange lines) and XBB.1.5 RBD (in maroon lines). (D) PRS sensor profiles for the BQ.1 RBD (in orange lines) and BQ.1.1 RBD (in maroon lines). The positions of Omicron mutational sites are indicated by brown-colored filled circles. The convergent mutation sites are indicated by yellow-colored filled diamonds.
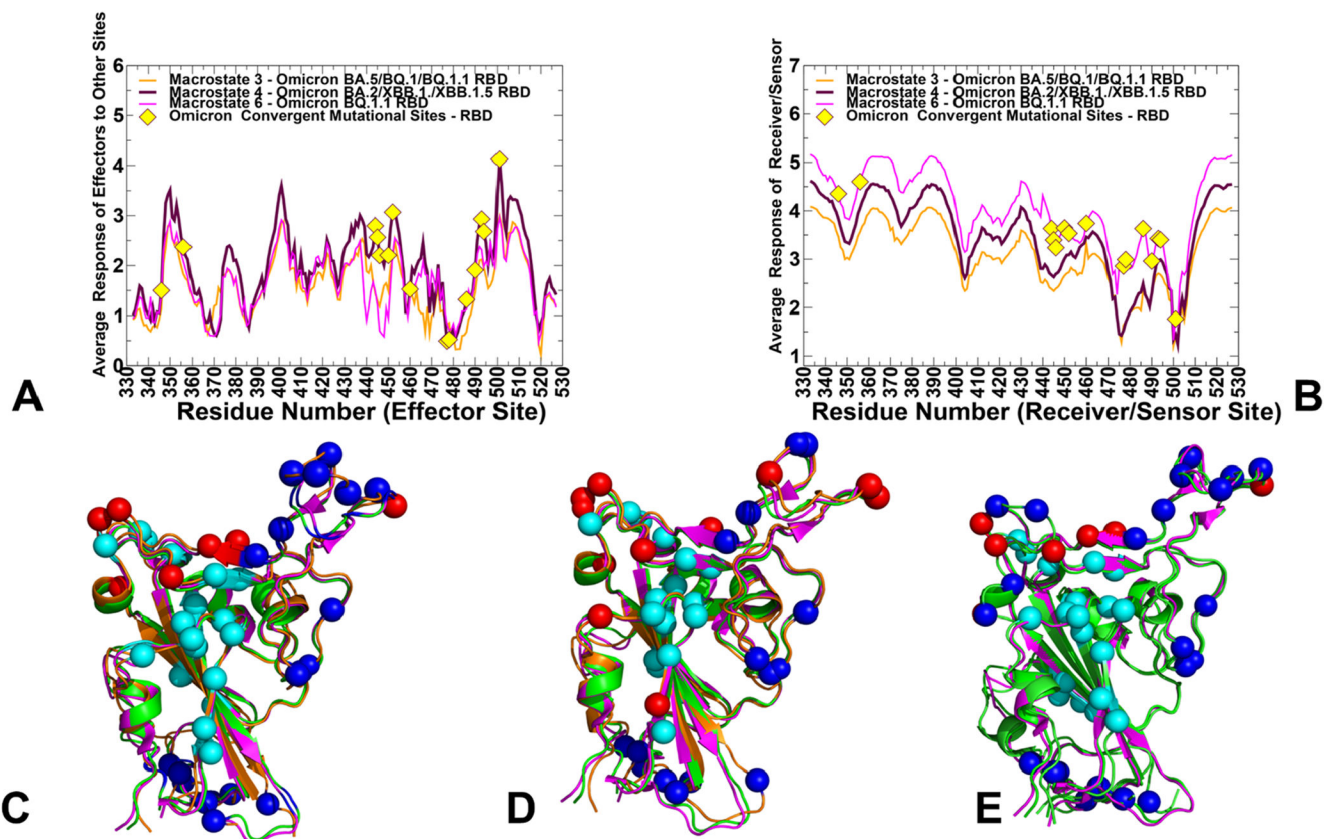
Figure 11.

PRS analysis of the macrostates for the Omicron RBD-ACE2 complexes. (A) PRS effector profiles for macrostate 3 (in orange lines), macrostate 4 (in maroon lines), and macrostate 6 (in magenta lines). (B) PRS sensor profiles for macrostate 3 (in orange lines), macrostate 4 (in maroon lines), and macrostate 6 (in magenta lines). The convergent mutation sites are indicated by yellow-colored filled diamonds. Structural mapping of the allosteric effector and sensor centers in macrostate 3 (C), macrostate 4 (D), and macrostate 6 (E). The RBD conformations for macrostates are shown in orange ribbons and overlayed with crystallographic BA.2 RBD conformation, pdb id 7XB0 (in green ribbons) and BA.5 RBD conformation, pdb id 7XWA (in magenta ribbons). The allosteric effector centers are shown in cyan spheres, and allosteric sensor centers are in blue spheres. The convergent mutation sites are shown in red spheres. Convergent mutation sites that correspond to the effector hotspots (K444T, N450, L452R, and Y501) are shown in cyan spheres and convergent mutation sites that correspond to sensor centers (T478R/K, E484K, and F486S/P) are accordingly in blue spheres.
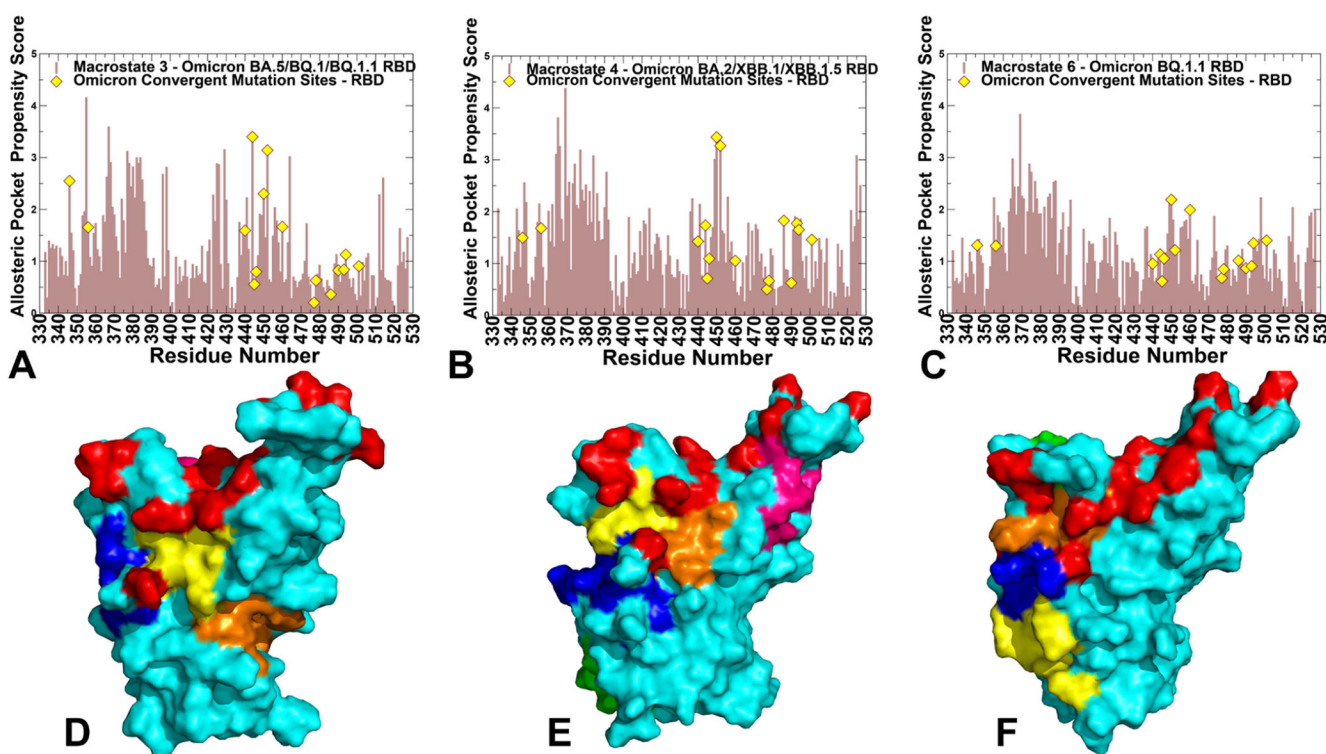
Figure 12.
Residue-based allosteric pocket propensity scores of the RBD residues are computed for representative RBD conformations corresponding to macrostate 3 (A), macrostate 4 (B), and macrostate 6 (C). The allosteric propensity profiles are in light brown bars. The convergent mutation sites (R346, K356, N440, K444, V445, G446, N450, L452, N460, T478, F486, F490, R493, and S494) are depicted in yellow-colored filled diamonds. Structural mapping of PASSer-predicted allosteric pockets on representative RBD conformations corresponding to macrostate 3 (D), macrostate 4 (E), and macrostate 6 (F). The RBD conformations are in the cyan surface, and convergent mutation sites are shown in red. All macrostates share the predicted RBD pocket (shown in blue surface) that is aligned with the experimentally known allosteric site (residues F338, F342, Y369, F371, A372, I434, and W436).

Table 1.

Mutational Landscape of the Omicron Subvariants in the S-RBD

Omicron variant	mutational landscape
BA.1	A67, T95I, G339D, S371L, S373P, S375F, K417N, N440K, G446S, S477N, T478K, E484A, Q493R, G496S, Q498R, N501Y, Y505H, T547K, D614G, H655Y, N679K, P681H, N764K, D796Y, N856K, Q954H, N969K, L981F
BA.2	T19I, G142D, V213G, G339D, S371F, S373P, S375F, T376A, D405N, R408S, K417N, N440K, S477N, T478K, E484A, Q493R, Q498R, N501Y, Y505H, D614G, H655Y, N679K, P681H, N764K, D796Y, Q954H, N969K
BA.2.75	T19I, G142D, K147E, W152R, F157L, I210V, V213G, G257S, G339H, S371F, S373P, S375F, T376A, D405N, R408S, K417N, N440K, G446N, S477N, T478K, E484A, Q498R, N501Y, Y505H, D614G, H655Y, N679K, P681H, N764K, D796Y, Q954H, N969K
XBB.1	T19I, V83A, G142D, Del144, H146Q, Q183E, V213E, G252V, G339H, R346T, L368I, S371F, S373P, S375F, T376A, D405N, R408S, K417N, N440K, V445P, G446S N460K, S477N, T478K, E484A, F486S, F490S, R493Q reversal, Q498R, N501Y, Y505H, D614G, H655Y, N679K, P681H, N764K, D796Y, Q954H, N969K
XBB.1.5	T19I, V83A, G142D, Del144, H146Q, Q183E, V213E, G252V, G339H, R346T, L368I, S371F, S373P, S375F, T376A, D405N, R408S, K417N, N440K, V445P, G446S, N460K, S477N, T478K, E484A, F486P, F490S, R493Q reversal, Q498R, N501Y, Y505H, D614G, H655Y, N679K, P681H, N764K, D796Y, Q954H, N969K
BA.4/BA.5	G339D, S371F, S373P, S375F, T376A, D405N, R408S, K417N, N440K, L452R, S477N, T478K, E484A, F486V, R493Q reversal, Q498R, N501Y, Y505H
BQ.1	G339D, S371F, S373P, S375F, T376A, D405N, R408S, K417N, N440K, K444T, L452R, N460K, S477N, T478K, E484A, F486V, R493Q reversal, Q498R, N501Y, Y505H
BQ.1.1	G339D, R346T, S371F, S373P, S375F, T376A, D405N, R408S, K417N, N440K, K444T, L452R, N460K, S477N, T478K, E484A, F486V, R493Q reversal, Q498R, N501Y, Y505H

Table 2.

Structures of the Omicron RBD-ACE2 Complexes Simulated in This Study

PDB	system	productive run per single simulation (μs)	number of simulations
7XB0	Omicron RBD BA.2-ACE2	1	3
7XWA	Omicron RBD BA.4/BA.5-ACE2	1	3
model	Omicron RBD XBB.1-ACE2	1	3
model	Omicron RBD XBB.1.5-ACE2	1	3
model	Omicron RBD BQ.1-ACE2	1	3
model	Omicron RBD BQ.1.1-ACE2	1	3